Barotropic Growth in Monsoon Depressions

Michael Diaz and William Boos

Department of Earth and Planetary Science, University of California, Berkeley, USA

Despite their significant impact on rainfall during the South Asian monsoon, there exists no widely accepted mechanism explaining the occurence of monsoon depressions over the Bay of Bengal. This study presents a hierarchy of numerical experiments aimed at finding such an explanation. Using a basic state-perturbation decomposition, we derive a system of equations which can represent the complex basic state characterizing the monsoon region. We find that modal solutions to these equations linearized about this basic state can explain many features of observed monsoon depressions, including their warm over cold core structure, westward propagation, and lower-tropospheric wind maximum. For the zonally symmetric case, these modes are barotropically unstable, drawing their energy from the meridional shear of the monsoon trough. For the zonally varying basic state, modal solutions still derive their energy through barotropic conversion, but fail to achieve positive net growth rates when dissipative processes are included. For the non-linear equation set, these modes can be forced by a heating impulse. Our results support the idea that barotropic instability can explain the structure, propagation, and geographic distribution of monsoon depressions, but not their rapid growth rates. We speculate that condensational heating coupled to these waves is needed for a positive growth rate.

1. Introduction

At first glance, Indian monsoon depressions appear to have much in common with standard tropical depressions: they typically form over warm water, have a deep, cyclonic circulation, and produce copious rainfall. However, in many ways they are quite different. For example, their circulation rarely achieves the intensity, symmetry, and small scale of the core of a mature tropical cyclone. Instead, it generally remains broad and weak with more loosely organized precipitation. Additionally, in contrast with the warm core of tropical depressions, which extends through the full depth of the troposphere, monsoon depressions have a low-level cold core underlying a warm core. Such a configuration is incompatible with the air-sea interaction mechanism by which tropical depressions are generally thought to intensify (Emanuel (1986)). In fact, monsoon depressions often form and strengthen over land, a feat rare for tropical depressions (Arndt *et al.* (2009)). Furthermore, being embedded within the larger-scale South Asian monsoon, they are often subjected to strong vertical wind shear, a well-known detriment to tropical cyclogenesis.

Based on these dissimilarities, one could reasonably argue that the mechanism by which monsoon depressions form and intensify differs from that of tropical depressions. It has long been recognized that the presence of horizontal and vertical wind shear associated with the large-scale monsoon circulation may lead to their growth through a dynamic instability process (e.g. Rao (1971), Krishnamurti *et al.* (1976)). However, there is little consensus as to how this mechanism would operate. Some have suggested that the flow is baroclinically unstable (Mishra and Salvekar (1980); Saha and Chang (1983); Salvekar and Mishra (1985); Salvekar *et al.* (1986)). However, Moorthi and Arakawa (1985) argue that the easterly vertical shear in this region is too weak to support baroclinic instability in the traditional sense. Instead, they propose that monsoon depressions arise through moist baroclinic instability, a process which requires condensational heating from precipitation as an additional energy source. A number of subsequent idealized modeling studies have made similar arguments (Krishnakumar *et al.* 1992; Kasture *et al.* 1993). Nevertheless, this explanation is still problematic, because baroclinic instability, whether dry or moist, requires that the disturbance tilt upshear with height (Cohen and Boos (2016)). Observed monsoon depressions by contrast generally exhibit either no tilt or a slightly downshear tilt (Hunt *et al.* 2016a; Cohen and Boos 2016). Some evidence even suggests that vertical shear is detrimental to their formation. For example, using statistical regression to model climatological genesis frequency of monsoon depressions, Ditchek *et al.* (2016) found that they occur less frequently where vertical wind shear is stronger.

Besides baroclinic instability, the monsoon trough's horizontal shear could be barotropically unstable. Exploration into this possibility has yielded mixed results. Many studies have cast doubt on this mechanism. For example, a linear instability analysis

by Shukla (1977) found that the most unstable normal mode of a basic state representative of the monsoon region has a westward phase speed of $15\,\mathrm{m\,s}^{-1}$ and maximum amplitude in the upper troposphere, both inconsistent with monsoon depressions, whose phase speed is typically westward near $3\,\mathrm{m\,s}^{-1}$ and whose strongest amplitude is in the lower troposphere. From this discrepancy, he concluded that barotropic instability cannot explain the occurence of monsoon depressions. Additionally, most of the studies in which moist baroclinic instability is the dominant growth mechanism find that barotropic energy conversion is small or negative (Krishnakumar *et al.* 1992; Kasture *et al.* 1993). A number of studies of the energetics of individual monsoon depressions seem to support these idealized modeling results. Krishnamurti *et al.* (2013) found that, for a sample of four monsoon depressions during the year 1996, energy is transferred from the perturbation flow to the zonal-mean flow, a direction indicative of decay through barotropic conversion. Rajamani (1985) and Rajamani and Sikdar (1989) came to similar conclusions for monsoon depressions during July 1963 and August 1979 respectively.

By contrast, other studies have found some evidence to support barotropic instability. For instance, Subrahmanyam *et al.* (1981) and Nitta and Masuda (1981) find barotropically unstable normal modes in the mid-tropospheric flow. However, in both of these studies, the phase velocity of these modes is eastward, which is opposite that typical of monsoon depressions. Additionally, Goswami *et al.* (1980) find barotropic instability in the mid-troposphere flow over western India, but find the flow over eastern India and southeast Asia, where monsoon depressions generally form, to be barotropically stable. Noting the conflicting results of previous studies, all of which use normal-mode instability theory, Lindzen *et al.* (1983) used a pulse asymtotics approach and found instabilities in the 500 mb flow with a wavelength of 2600 km and westward phase speed of 1.5 ms^{-1}, both in comparably good agreement with typical values. Barotropic instability also has some observational support. Ditchek *et al.* (2016) found low-level absolute vorticity, of which the horizontal shear of the monsoon trough is a large component, to be an important variable in their regression model of genesis frequency. Several case studies find barotropic conversion to be an energy source for monsoon depressions, though secondary to energy from cumulus convection (Krishnamurti *et al.* 1976; Nagar *et al.* 2009). More recently, Mishra (2018) find that the monsoon trough becomes increasingly barotropically unstable preceding monsoon depression formation.

Regardless of how relevant the background shear may be, most studies conclude that moist convection plays an essential role in monsoon depression growth. For instance, in a modeling study of an observed monsoon depression, Krishnamurti *et al.* (1976) found that its primary energy source was from diabatic heating generated by cumulus convection. Additionally, three of the four variables used in the genesis index of Ditchek *et al.* (2016) relate to how favorable the environment is for moist convection. However, incorporating this aspect of monsoon depression dynamics into the framework of linear instability theory has proven difficult. Some studies have argued that conditional instability of the second kind (CISK) may apply to monsoon depressions. Shukla (1978) considered CISK and found maximum growth rates at the smallest scale and significant discrepancies with observed monsoon depressions (their Fig. 6). However, since the time of these studies, the CISK mechanism itself has been discredited (refer to Montgomery and Smith (2014) for an overview) and thus any explanation relying on CISK should be treated with skepticism. Additionally, even if cumulus convection is the main energy source, it does not explain why monsoon depressions form here and not elsewhere. More recently, Adames and Ming (2018a) explain monsoon depression growth through a moisture-vortex instability which exists due to horizontal moisture advection and whose primary energy source is diabatic heating from convection.

Although it is possible that one of the aforementioned growth processes generates monsoon depressions *in situ*, some studies have argued that the initial disturbance can arise through a different physical process. For example, Krishnamurti *et al.* (1977) proposed that some may originate from energy dispersed from disturbances in the western Pacific. Others have suggested that many of them originate directly from western Pacific low pressure systems which propagate westward into the Bay of Bengal (Saha *et al.* (1981); Chen and Weng (1999)). Even if these mechanisms are correct, they do not explain their localization and rapid growth in the vicinity of the Bay of Bengal.

Judging by the wide variety of results and conclusions of previous studies, there is still no widely agreed-upon explanation for how monsoon depressions form. Why do so many discrepancies exist in the past literature on monsoon depressions? One source of disagreement may lie with the various ways in which the governing equations are simplified. Many studies use two-dimensional models which consider the horizontal or vertical shear independently. Others use quasi-geostrophic models with only a few vertical levels. Nearly all linearize their governing equations. Another problem may be that the assumption of scale separation between the basic state and the disturbance underlying the normal-mode instability approach undertaken in many of these studies is violated. Given that the wavelength of the disturbances is nearly the same length as the monsoon trough which is intended to be a basic state, it is questionable how well representative a zonally symmetric basic state is. Furthermore, results could be sensitive to the choice of basic state. The large-scale flow in the vicinity of the Bay of Bengal can vary substantially from day to day and it is not obvious how to specify a basic state which favors monsoon depressions. Finally, it is difficult to incorporate the impact of diabatic heating from convection into these models. As such, the treatment of convection in previous studies has been highly simplified and may be unrealistic.

The goal of our study is to work toward an explanation of how monsoon depressions form using a series of idealized numerical modeling experiments of increasing complexity. As with many previous studies, we start from the assumption that the background flow of the monsoon is important for their growth and model them as perturbations growing on this flow. However, we will derive an equation set which minimizes any simplifying assumptions and allows for three-dimensional variations in the perturbation and basic state flow which can accomodate the complex monsoon background flow. We will also more carefully construct a basic state representative of the environment in which monsoon depressions grow using a modern reanalysis product. Although we neglect condensation heating from convection, which many studies have noted to be important, our results suggest that many aspects of monsoon depressions can be explained without it.

This study is outlined as follows: Section 2 presents a derivation of our governing equation set and how we construct a representative basic state, Secs. 3 and 4 present a linear instability analysis of the zonally symmetric and zonally varying basic state respectively, Sec. 5 presents an initial value problem using the non-linear equation set, and Sec. 6 summarizes our results.

2. Methods

Here we derive a closed equation set which describes the time evolution of a perturbation on a three-dimensional time-independent basic state. Although the derivation is for the non-linear case, we will linearize it for some of our experiments.

2.1. Model Equations

100 The equations of motion on a dry, rotating atmosphere in Cartesian height coordinates can be expressed as

$$\frac{\partial \mathbf{u}}{\partial t} + \mathbf{u} \cdot \nabla \mathbf{u} = -\frac{1}{\rho}\nabla p - g\hat{\mathbf{k}} - f\hat{\mathbf{k}} \times \mathbf{v} + \mathbf{S} \tag{1a}$$

$$\frac{\partial \theta}{\partial t} + \mathbf{u} \cdot \nabla \theta = S_\theta \tag{1b}$$

$$\frac{\partial \rho}{\partial t} + \nabla \cdot (\rho \mathbf{u}) = 0 \tag{1c}$$

$$\theta = T(\frac{p_r}{p})^{\frac{R}{c_p}} \tag{1d}$$

$$p = \rho R T \tag{1e}$$

101 where $\mathbf{u} = \langle u, v, w \rangle$, $\mathbf{v} = \langle u, v \rangle$, $\mathbf{S}$ is a momentum source, S_θ is a heat source, f is the Coriolis parameter, which varies as a function
102 of latitude, and all other symbols have their usual meaning.

We first partition the thermodynamic fields into a vertically varying base state and a perturbation,

$$\rho = \rho_0(z) + \tilde{\rho}(\mathbf{r}, t) \tag{2a}$$

$$p = p_0(z) + \tilde{p}(\mathbf{r}, t) \tag{2b}$$

$$\theta = \theta_0(z) + \tilde{\theta}(\mathbf{r}, t) \tag{2c}$$

103 where $\mathbf{r} \equiv \langle x, y, z \rangle$. We then make the anelastic approximations whereby we assume that the base state values are much larger than
104 the perturbations and replace density by its base state except where it multiplies gravity. From these assumptions, we can derive the
105 following equations:

$$\frac{\partial \mathbf{u}}{\partial t} + \mathbf{u} \cdot \nabla \mathbf{u} = -\nabla \tilde{\phi} - g\frac{\tilde{\theta}}{\theta_0}\hat{\mathbf{k}} - f\hat{\mathbf{k}} \times \mathbf{v} + \mathbf{S} \tag{3a}$$

$$\frac{\partial \tilde{\theta}}{\partial t} + \mathbf{u} \cdot \nabla \tilde{\theta} + w\frac{\partial \theta_0}{\partial z} = S_\theta \tag{3b}$$

$$\nabla \cdot (\rho_0 \mathbf{u}) = 0 \tag{3c}$$

106 where $\tilde{\phi} \equiv \frac{\tilde{p}}{\rho_0}$. A full derivation from the standard equation set to the anelastic can be found in Sec. 2 of Bannon (1995). For our
107 purposes, the anelastic equation set has several advantages. First, it filters out acoustic waves, which require prohibitively small time
108 steps to solve. Second, it eliminates Eqs. 1d and 1e, whose partitioning into a basic state and perturbation is complicated and difficult to
109 linearize. Finally, because it remains non-hydrostatic, it can be extended to high-resolution convection resolving simulations in future
110 work.

Each of the fields can be partitioned into a time-independent basic state and a time-dependent perturbation. Let

$$\mathbf{u} = \bar{\mathbf{U}}(\mathbf{r}) + \mathbf{u}'(\mathbf{r}, t) \tag{4a}$$

$$\tilde{\phi} = \bar{\Phi}(\mathbf{r}) + \phi'(\mathbf{r}, t) \tag{4b}$$

$$\tilde{\theta} = \bar{\theta}(\mathbf{r}) + \theta'(\mathbf{r}, t) \tag{4c}$$

$$\mathbf{S} = \bar{\mathbf{S}}(\mathbf{r}) + \mathbf{s}'(\mathbf{r}, t) \tag{4d}$$

$$S_\theta = \bar{S}_\theta(\mathbf{r}) + s'_\theta(\mathbf{r}, t) \tag{4e}$$

111 where terms with overbars represent the basic state and terms with primes the perturbation.
112 Substituting Eq. 4 into Eqs. 3a, 3b, and 3c yields

$$\frac{\partial \mathbf{u}'}{\partial t} + (\bar{\mathbf{U}} + \mathbf{u}') \cdot \nabla(\bar{\mathbf{U}} + \mathbf{u}') =$$
$$-\nabla(\bar{\Phi} + \phi') + g(\frac{\bar{\theta} + \theta'}{\theta_0})\hat{\mathbf{k}} - f\hat{\mathbf{k}} \times (\bar{\mathbf{V}} + \mathbf{v}') + \bar{\mathbf{S}} + \mathbf{s}' \tag{5a}$$

$$\frac{\partial \theta'}{\partial t} + (\bar{\mathbf{U}} + \mathbf{u}') \cdot \nabla(\bar{\theta} + \theta') + (\bar{W} + w')\frac{\partial \theta_0}{\partial z} = \bar{S}_\theta + s'_\theta \tag{5b}$$

$$\nabla \cdot (\rho_0(\bar{\mathbf{U}} + \mathbf{u}')) = 0 \tag{5c}$$

113 In order for the basic state to remain stationary, it must be a time-independent solution to Eqs. 3a, 3b, and 3c. This constraint implies
114 that

$$\bar{\mathbf{U}} \cdot \nabla \bar{\mathbf{U}} = -\nabla \bar{\Phi} + g\frac{\bar{\theta}}{\theta_0}\hat{\mathbf{k}} - f\hat{\mathbf{k}} \times \bar{\mathbf{V}} + \bar{\mathbf{S}} \tag{6a}$$

$$\bar{\mathbf{U}} \cdot \nabla \bar{\theta} + \bar{W}\frac{\partial \theta_0}{\partial z} = \bar{S}_\theta \tag{6b}$$

$$\nabla \cdot (\rho_0 \bar{\mathbf{U}}) = 0 \tag{6c}$$

Equations 6a, 6b, and 6c are the governing equations for the basic state. In this context, $\bar{\mathbf{S}}$ and $\bar{S}_\theta$ are the momentum and heat sources necessary to keep basic state time-independent. Subtracting Eqs. 6a, 6b, and 6c from Eqs. 5a, 5b, and 5c respectively and rearranging yields the following:

$$\frac{\partial \mathbf{u}'}{\partial t} = -(\bar{\mathbf{U}} + \mathbf{u}') \cdot \nabla \mathbf{u}' - \mathbf{u}' \cdot \nabla \bar{\mathbf{U}} - \nabla \phi' + g\frac{\theta'}{\theta_0}\hat{\mathbf{k}} - f\hat{\mathbf{k}} \times \mathbf{v}' + \mathbf{s}' \tag{7a}$$

$$\frac{\partial \theta'}{\partial t} = -(\bar{\mathbf{U}} + \mathbf{u}') \cdot \nabla \theta' - \mathbf{u}' \cdot \nabla \bar{\theta} - w'\frac{\partial \theta_0}{\partial z} + s'_\theta \tag{7b}$$

$$\nabla \cdot (\rho_0 \mathbf{u}') = 0 \tag{7c}$$

Finally, we use Eqs. 7a and 7c to derive a diagnostic equation for ϕ'. Multiplying Eq. 7a by ρ_0, taking its divergence, and using Eq. 7c to remove the time derivative yields

$$\frac{\partial^2 \phi'}{\partial x^2} + \frac{\partial^2 \phi'}{\partial y^2} + \frac{\partial}{\partial z}(\rho_0 \frac{\partial \phi'}{\partial z}) = \nabla \cdot (\rho_0 G\{\mathbf{u}'\}) \tag{8}$$

where the operator G includes all of the terms on the right-hand side of Eq. 7a except for those involving pressure gradients. This is a version of the anelastic pressure equation. Equations 7a, 7b, and 8 form a set of five equations and five unknowns (u', v', w', θ', ϕ') which we can solve using standard numerical methods. The terms $\mathbf{s}'$ and s_θ will be either specified or expressed in terms of the other variables.

2.2. *Numerical Methods*

To solve our equation set (i.e. Eqs. 7a, 7b, and 8), the required field are discretized onto a staggered C-grid (cite), where the velocity components occupy the faces of a control volume and all scalars occupy the center of the control volume. To solve numerically, all advection terms in Eqs. 7a and 7b are expressed in flux form, which has better mass conserving properties compared to advective form. Advection of a generic variable q can be expressed as

$$\mathbf{u} \cdot \nabla q = \frac{1}{\rho_0}[\nabla \cdot (\rho_0 q\mathbf{u}) - q\nabla \cdot (\rho_0 \mathbf{u})] \tag{9}$$

Using Eq. 3c to eliminate the second term on the right-hand side of Eq. 9 yields

$$\mathbf{u} \cdot \nabla q = \frac{\partial(qu)}{\partial x} + \frac{\partial(qv)}{\partial y} + \frac{1}{\rho_0}\frac{\partial(\rho_0 qw)}{\partial z} \tag{10}$$

The horizontal and vertical spatial derivatives are evaluated using an upwind-biased 5th-order and 3rd-order accurate scheme respectively. Time derivaties use a 3rd-order accurate Runge-Kutta scheme. Details of these methods are given in Wicker and Skamarock (2002).

Solving Eq. 8 directly would lead to a gradual accumulation of numerical error in the divergence field due to the finite precision of floating-point arithmetic. To get around this problem, we adapt a version of the projection method originally proposed by Chorin (1968). In the first step, an intermediate velocity field $\mathbf{u}^*$ is calculated at time n by integrating all of the terms in Eq. 7a except for the pressure gradient term for one time step Δt.

$$\mathbf{u}^* = \mathbf{u}'_\mathbf{n} + G\{\mathbf{u}'_\mathbf{n}\}\Delta t \tag{11}$$

Eq. 8 is then solved for ϕ' using $\mathbf{u}^*$ in place of $G\{\mathbf{u}'\}$. This solution requires inverting the three-dimensional Laplacian operator. To do this efficiently, we use a method based on Fast Fourier transforms in the horizontal direction and Gaussian elimination in the vertical. The lateral boundary condition is periodic and the upper and lower are zero pressure gradient. Since the prognostic variables are damped to zero at the lateral boundaries, they are effectively zero-gradient also.

The final velocity is then calculated by

$$\mathbf{u}'_{\mathbf{n+1}} = \mathbf{u}^* + \nabla \phi' \Delta t \tag{12}$$

2.3. *Boundary Conditions*

At the lateral boundaries, the perturbation is damped to zero according to the following equation:

$$q'_{n+1} = q'_n - q'_n\frac{1}{2}[1 - cos(\frac{b\pi}{B})] \tag{13}$$

where q' is a generic variable, B is the width of the boundary, and b is the distance from the lateral boundary. At the upper and lower boundary, the vertical velocity and pressure gradient are set to zero. A damping layer is placed at the upper boundary whose primarily function is to damp out gravity waves.

2.4. Basic State

To be relevant to monsoon depressions, the basic state flow (i.e. $\bar{U}$, $\bar{V}$, $\bar{W}$, and $\bar{\theta}$) must represent the environment in which they typically form and grow. One approach would be to use a time mean of these fields over South Asia during the summer monsoon. However, because the flow over this region can vary substantially from day to day, this time mean would combine many different flow configurations and potentially yield an overly-smoothed basic state. Following the assumption that environmental wind shear is important for monsoon depression growth, this outcome is unsatisfactory. As many of the possible atmospheric states in this region may not even support monsoon depression growth, a better approach would be to use an average from environments in which monsoon depressions actually formed. However, this alternative creates a second problem: such an average may be overly influenced by the monsoon depressions themselves. Keeping these issues in mind, our procedure for constructing a basic state attempts to satisfy the competing goals of averaging out small-scale noise, retaining the strong shear of the monsoon trough, and minimizing the impact of monsoon depressions on the average.

To find environments which favor monsoon depressions, we use the monsoon depression track dataset of Hurley and Boos (2015). We select all monsoon depressions which formed in the rectangle bounded by $17°$N, $23°$N, $85°$E, and $100°$E during June through September from 1979 to 2009. These criteria lead to 64 cases. Each case is then paired with the corresponding fields from the ERA-interim reanalysis (Dee *et al.* (2011)), which is available every six hours. We then construct a basic state for each case using a short-term average. Attempting to exclude the monsoon depressions, we first tried averaging the 24 hours preceding the genesis time identified by the tracking algorithm. However, new monsoon depressions are preceded by older ones with enough frequency to leave an imprint of the previous monsoon depression in the time-mean fields. We thus decided upon averaging the 24 hours following and including genesis (i.e. five individual times per case). During this period, the initial disturbance found by the tracking algorithm tended to be weak enough not to leave a significant vortex in the time-mean fields.

Even with these constraints, the basic states vary substantially. Some of this variability results from the monsoon trough moving north and south. Another problem is that the starting point identified by the algorithm may be well before the time period of most significant growth. Following our goal of avoiding averaging dissimilar basic states, we perform an Empirical Orthogonal Function (EOF) analysis on them before averaging them together. For the set of 64 basic states derived above, we compute an EOF of the the zonal wind within a volume bounded by $13.7°$N, $29.1°$N, $72.4°$E, $102.7°$E, 550 hPa, and 875 hPa. The first EOF, which explains 35.8% of the variance, corresponds to the monsoon trough moving north and south or strengthening and weakening. Using the EOF time series, we average the phase of this EOF which corresponds to well developed easterly flow to the north of the monsoon westerlies, a pattern indicative of a well-defined monsoon trough. This restriction reduces our total number of cases to 31 and ultimately leads to averaging 155 individual times into our basic state. The result is shown in Fig. 1. Consistent with our aim, it has a well-developed monsoon trough and much of the small-scale noise has been averaged out.

2.5. Energetics Equation

To gain physical insight into how perturbations interact with the basic state, it is useful to derive an equation for the kinetic energy of the horizontal perturbation wind. Taking the dot product of the horizontal velocity vector **v** with the horizontal components of Eq. 7a yields,

$$\frac{\partial K_e}{\partial t} + (\bar{\mathbf{U}} + \mathbf{u}') \cdot \nabla K_e +$$
$$u'v'\frac{\partial \bar{U}}{\partial y} + u'v'\frac{\partial \bar{V}}{\partial x} + u'^2\frac{\partial \bar{U}}{\partial x} + v'^2\frac{\partial \bar{V}}{\partial y} + u'w'\frac{\partial \bar{U}}{\partial z} + v'w'\frac{\partial \bar{V}}{\partial z}$$
$$= -\mathbf{v}' \cdot (\frac{\partial \phi'}{\partial x}\hat{\mathbf{i}} + \frac{\partial \phi'}{\partial y}\hat{\mathbf{j}}) + \mathbf{v}' \cdot (s_u'\hat{\mathbf{i}} + s_v'\hat{\mathbf{j}}) \quad (14)$$

where $K_e \equiv \frac{u'^2 + v'^2}{2}$ is the perturbation kinetic energy. The first two terms on the left-hand side are the local rate of change and advection by the mean and perturbation flow. The next six terms are exchanges between the kinetic energy of the mean flow and the perturbation. The first term on the right-hand side of the equation is the work done by the pressure gradient force. As shown by Orlanski and Chang (1993), this term can be decomposed into the baroclinic term, which is associated with warm air rising and cold air sinking, and a boundary pressure work term. Since the standard baroclinic term is not strictly valid on a limited domain, we use the pressure work term directly. The final term in Eq. 14 is frictional dissipation.

3. Linear Normal Modes (Exp. A)

For many types of disturbances which can be thought of as perturbations growing on a background flow, linear normal-mode instability theory has proven to be a useful starting point for understanding their growth and structure. However, as noted in the introduction, this method has proven more difficult when applied to monsoon depressions. In this experiment (Exp. A), we will revisit this theory by finding normal mode solutions to our equation set linearized about the basic state we have constructed from reanalysis data.

3.1. Experimental Design

We linearize Eqs. 7a, 7b, and 8 by eliminating all of the quadratic terms. We also remove zonal variations in our basic state by considering only meridional cross sections at a particular longitude. Further details about the specific model settings are listed in Tab. 6. The desired normal-mode solutions to this system of linearized equations take the form

$$\psi'(\mathbf{r}, t) = \hat{\psi}(y, z)e^{i(kx - \omega t)} = \hat{\psi}(y, z)e^{ikx}e^{-i\omega t} \quad (15)$$

where ψ' represents a perturbation and all other variables have their standard meaning. To reach this solution, we initialize with random noise and integrate forward in time. During this integration, the zonal structure of ψ' is constrained to e^{ikx} using a discrete Fourier transform to isolate a single wavenumber of interest at every time step. To maintain the perturbation fields within a physically realistic range, they are periodically rescaled by a constant. The structure $\hat{\psi}(y,z)e^{-i\omega t}$ which maximizes the growth rate will eventually emerge with a sufficiently long integration time. Besides examining their structure, we also want to compare the growth rates for a wide range of normal modes with closely spaced wavelengths. Noting that $L_x = N_x \frac{\Delta x}{k}$, where L_x is the zonal wavelength, N_x the number of grid points in the zonal direction, and Δx the horizontal grid spacing, and that N_x and k can only take on integer values, this requires a large value of N_x and is computationally expensive. Therefore, instead of varying k to get different wavelengths, we hold k constant at wavenumber 2 and vary N_x.

We add the following two physical parameterizations to Eq. 7a and 7b to represent dissipative processes,

$$\mathbf{s}' = -s_0(z)(u'\hat{\mathbf{i}} + v'\hat{\mathbf{j}}) + [\alpha_y \frac{\Delta x^6}{\Delta t}]\frac{\partial^6 \mathbf{u}'}{\partial y^6} + \alpha_z [\frac{\Delta z^6}{\Delta t}]\frac{\partial^6 \mathbf{u}'}{\partial z^6} \tag{16a}$$

$$\mathbf{s}'_\theta = [\alpha_y \frac{\Delta x^6}{\Delta t}]\frac{\partial^6 \theta'}{\partial y^6} + \alpha_z [\frac{\Delta z^6}{\Delta t}]\frac{\partial^6 \theta'}{\partial z^6} \tag{16b}$$

where the values of the constants s_0 and α are given in Tab. 6 and s_0 is zero everywhere except at the lowest model level, which is located $250m$ above the surface. The first term on the right hand side of Eq. 16 represents near-surface friction. Including friction is essential because it has been found to have an important stabilizing effect for a variety of atmospheric disturbances (e.g. Hall and Sardeshmukh (1998), Hall *et al.* (2006)). The other terms represent 6th-order diffusion. Although the upwind-biased scheme we use to evaluate the spatial derivatives contains implicit 6th-order diffusion which is a function of the Courant number (Wicker and Skamarock 2002), our linearizing of the equation set and setting $\bar{V}$ and $\bar{W}$ to zero eliminates this diffusion in the meridional and vertical direction. Excluding this process leads to the meridional and vertical wavelength of the disturbance collapsing to the grid scale near the zero-wind line of the basic state flow, a location where the assumption of linearity first becomes invalid. This diffusion crudely approximates the tendency for these smaller-scale waves near the zero-wind line to break and reduce the shear in the perturbation flow.

Though we will discuss the results from other longitudes, we focus most of our analysis on $87^\circ E$, which is located near the maximum track density (Fig. 2 in Hurley and Boos (2015)). Figure 2 shows a latitude-height cross section of the basic state zonal winds and potential temperature (Fig. 2a) and the basic state absolute vorticity (Fig. 2b). The terrain is outlined in brown. The monsoon trough axis, as identified by the zero wind line between 20°N and 25°N, is associated with a maximum in absolute vorticity. As suggested by previous studies, the resulting absolute vorticity gradient reversal could be barotropically unstable. Additionally, the shift from westerly monsoon flow at low levels to easterly flow in the upper troposphere associated with the Tropical Easterly Jet leads to strong vertical wind shear. As noted previously, its presence has led some to suggest that monsoon depressions may arise through baroclinic instability.

Several complications arise from using this basic state flow as given. One problem is the fictitious data below the topography. If included, the most unstable normal mode grows on the unphysical temperature gradients at the edge of the Himalayas. To resolve this, we set the basic state zonal wind and potential temperature to a constant value north of the blue line in Fig. 2b equal to the value at the blue line. Another problem is that the most unstable normal mode for the range of basic states and wavelengths we use does not always correspond to monsoon depressions. At wavelengths longer than 3500 km, upper tropospheric waves dominate, and at wavelengths shorter than about 1000 km, waves grow near the surface along 10°N. To exclude these wave modes, we extend the model's upper and lateral boundaries as far as needed to damp these instabilities, as shown by the dotted lines in Fig. 2b. Unfortunately, the upper-level damping comes uncomfortably close the lower-tropospheric modes we are trying to isolate. For the part of our analysis where we show the structure of the wave modes, we present results for wavelengths short enough that upper-level damping is not required. For experiments which vary the wavelength and longitude, it is included.

3.2. Results

Results are shown in detail for the 87°E basic state for the normal mode of wavelength 3200 km, which is shorter than the most unstable mode but longer than that typical of monsoon depressions. Its horizontal structure in terms of pressure (p'), wind ($\mathbf{v}'$), and vertical velocity (w') is shown in Fig. 3. It consists of a series of cyclones and anticyclones which tilt against the basic state meridional shear, a configuration suggestive of barotropic instability. Their maximum amplitude lies near 25.7°N, which, given their westward phase velocity of $1.7\,\mathrm{m\,s}^{-1}$, is located near the critical layer of this basic state flow. Although this latitude is north of the observed maximum track density for monsoon depressions, which is located between 20°N and 23°N for 87°E (Fig. 1 in Hunt *et al.* (2016a)), significant amplitude does extend farther south. The pattern of ascent located west of the trough axis and descent to its east is broadly consistent with that of observed monsoon depressions.

The vertical structure of the the disturbance is depicted in Fig. 4, which shows a longitude-height cross section of the meridional wind (v') and potential temperature (θ') at (a) 25.7°N and (b) 21.2°N. The former is centered at the disturbance's maximum amplitude and the latter near where monsoon depressions more commonly track. Consistent with observed monsoon depressions, both cross sections have a warm over cold core with a low-level wind maximum. However, the 3.75 km altitude of the warm core at 25.7°N is much lower than the more typically observed value of 7-8 km (Fig. 13 in Hunt *et al.* (2016b)). The minimal to slightly downshear tilt with height indicates that these disturbances are not baroclinically unstable. In fact, most of their amplitude is confined to below the strong shear aloft and north of the stronger vertical shear to the south.

Following the same procedure as above for different wavelengths using the 87°E basic state, we calculate zonal phase velocity, period, and growth rate as a function of wavelength and use Eq. 14 to partition the growth rate into different physical processes (Fig. 5). For a wide range of wavelengths, the meridional shear of the basic state zonal wind is barotropically unstable with the $u'v'd\bar{U}/dy$ term contributing up to $0.62day^{-1}$ to the growth rate (Fig. 5b). The net growth rate, however, is much lower with friction and diffusion (Eq. 16) consuming a large quantity of energy. Diffusion, being scale selective, becomes an increasingly large energy sink

as the wavelength shortens. As this diffusion is not applied in the zonal direction, this trend reflects the meridional and vertical scales becoming smaller. The zonal wavelength is, however, impacted by the diffusion implicit in the upwind-biased numerical advection scheme. This contributes to the residual becoming sharply negative at short wavelengths. The pressure work term being negative for most wavelengths is consistent with a lack of baroclinic instability. In total, there are multiple physical process which can contribute to pressure work. One negative source comes from the energy needed to create the temperature perturbations. As the wind perturbations grow by extracting energy from the basic state meridional shear, the temperature field needed to keep the resulting disturbance in approximate thermal wind balance requires that some of this kinetic energy be converted to potential energy through rising cool air and sinking warm air. This process has some support from observations as the central region of observed monsoon depressions is in fact associated with sinking warm air (cite). Additionally, the presence of surface friction causes the low-level winds to point down the pressure gradient, converting potential energy to kinetic. Finally, given the presence of a basic state temperature gradient, it is possible that some energy is drawn from the basic state available potential energy. Interestingly, at shorter wavelengths, the pressure work becomes strongly positive. One source of this change is simply the rapid loss barotropic conversion at shorter wavelengths. We also note that the smaller-scale disturbances become increasingly concentrated to the north, where the surface baroclinic zone is slightly stronger.

Figure 5a shows the phase velocity and period as a function of wavelength. The phase speed is westward for all wavelength and decreases with increasing wavelength until around 4000 km. Afterwards it increases slightly before leveling off. Plots of the shorter wavelengths (not shown) reveal that they are increasingly embedded within the easterly flow to the north, a shift which would increase their westward phase speed. For wavelengths characteristic of monsoon depressions, the zonal phase velocity is between about -2.5 to $-1.8\,m\,s^{-1}$. By comparison, Boos *et al.* (2017) calculated a mean value of $-1.5\,\mathrm{m\,s^{-1}}$ and a mode value of $-3.4\,\mathrm{m\,s^{-1}}$.

We repeat the procedure described in Sec. 3.1 to find normal mode solutions of 3200 km wavelength for a wide range of longitudes. To accomodate for the shifting latitude of the steepest topography and the $10°$N instability moving northward for longitudes farther west, the boundary conditions and cut-off line (see Fig. 2) are shifted for each longitude following a similar logic as before (list in table?). Figure 6 shows the growth rate as a function of longitude partitioned into different physical processes based on Eq. 14. This analysis reveals a wide range of longitudes which can support barotropic instability with a sharp cutoff corresponding to the eastern and western edges of the monsoon trough (Fig. 1). As before, the net growth rate is much smaller due to the effects of friction and diffusion. Although not shown, we note that normal modes obtained using basic states between $78°$E and $92°$E look very similar to those at $87°$E discussed previously. However, west of this range, their structure changes. Between $74°$E and $78°$E, they become increasingly elevated. This is reflected in the friction term becoming nearly zero and the pressure work term becoming strongly negative, a consequence of the loss of the positive source caused by low-level friction turning the wind down the pressure gradient. West of $74°$E, the modes become increasingly baroclinic and surface intensified, exhibit an eastward phase velocity, and have little resemblance to those farther east. With this in mind, it is reasonable to conclude that the region which can support barotropic instability is approximately $20°$ (2200 km) long. The fact that this value is comparable to the wavelength of the most unstable normal modes (Fig. 5) motivates the next part of this study.

4. Zonally Varying Basic State (Exp. B)

As demonstrated in Exp. A, the longitudinal extent of the region which can support barotropic instability is of similar scale to or slightly shorter than the wavelengths at which normal modes grow fastest. With little separation between these two scales, it is questionable how well a zonally symmetric basic state represents waves which can grow in the monsoon environment. In this experiment (Exp. B), we consider how zonal variations in the basic state impact the growth and structure of wave-like solutions to our linearized equation set.

4.1. Experimental Design

Instead of the single-wavelength normal modes of Exp. A, solutions now consist of cyclically repeating structures of the form

$$\psi'(\mathbf{r}, t) = e^{\sigma t}[A(\mathbf{r})sin(\omega t) + B(\mathbf{r})cos(\omega t)] \tag{17}$$

where σ is the growth rate and $A(\mathbf{r})$ and $B(\mathbf{r})$ represent two spatially orthogonal structures (Simmons *et al.* 1983; Hall and Sardeshmukh 1998). These solutions constitute the eigenmodes of our system of equations linearized about the zonally varying basic state. Over the course of one wave period ($\frac{1}{\omega}$), they oscillate from A to B to $-A$ to $-B$ and then back again. As in Exp. A, over a sufficiently long integration time, the solution will converge to the fastest growing or slowest decaying eigenmode, depending on the sign of σ. Throughout the integration, we rescale the prognostic variables by a constant to keep them close to observed values. Although not strictly necessary with a linearized equation set, having the fields approach extremely large or small values is undesirable for practical purposes. The terms $\mathbf{s}'$ and s'_θ are the same as in Exp. A except for the sixth-order diffusion now acting in three dimensions instead of two.

As in Exp. A, we have to somehow account for the presence of topography and the artificial data beneath it. Since the technique used before does not extend well to zonal variations in topography, we take a different approach: the top faces of the control volumes lying just beneath the physical terrain are treated as the surface and the component of the fluxes in Eq. 10 orthogonal to the sides of the control volumes directly adjacent to the terrain are set to zero. This implementation leads to a stair-step like terrain. Although not optimal for simulating flow over complex topography, the fact that its effects on the basic state are already included in the reanalysis mitigates some of the drawbacks to this approach.

A second problem we encountered was that the small-scale spatial variability in the basic state leads to small-scale waves with higher growth rates than the ones are interested in. This problem is exacerbated by the presence of topography and the many regions of weak basic state flow. To damp these waves in favor of larger-scale ones, we increase the scale-selective 6th-order diffusion compared to the previous experiment (Tab. 6). Similar solutions can be reached with smaller amounts of diffusion, though they become increasingly contaminated with small-scale noise.

Finally, it is worth mentioning that, unlike in Exp. A, no upper-level modes appear in this basic state. As noted in the introduction, several studies found a most unstable mode in the upper-tropospheric flow (Shukla 1978; Goswami *et al.* 1980). This experiment suggests that they were artifacts of zonal symmetry.

4.2. Results

In contrast with Ex. A, the zonally varying basic state has no amplifying modal solutions. Hence, the structure which emerges after a sufficiently long integration is the slowest-decaying eigenmode. The time evolution of its pressure (p') and wind ($\mathbf{v}'$) over one wave period (12.7 days) overlaid with the basic state zonal wind ($\bar{U}$) is shown in Fig. 7. It forms a localized wave packet centered near the northernmost Bay of Bengal whose individual phases move northwestward along the monsoon trough axis. The individual circulation centers closely follow the path of observed monsoon depressions and, with their upshear tilt, bear some resemblance to the modal solutions in Exp. A. This similarity is especially apparent on days 0 and 6 when they are centered within the maximum meridional shear. Significant wave amplitude also extends into regions east of $91°$E. Considering the rapid dropoff in barotropic growth rates (Fig. 6) and their lack of upshear tilt, this extension is likely a dispersion phenomenon. With a poleward directed absolute vorticity gradient (Fig. 2a) and westerly low-level flow (Fig. 1), the Rossby wave group velocity is eastward, in agreement with the results of Adames and Ming (2018b). Besides the monsoon depression-like wave modes, additional waves appear east of $100°$ associated with another wind shift line in the western Pacific (Fig. 1). These may correspond to easterly waves.

Figure 8 shows a cross section of the perturbation wind and potential temperature (θ') of the cyclonic phase of the wave at day 5, when it is centered near $87°$E, the focus longitude of Exp. A. To account for its tilted structure, these fields are rotated $30°$ counterclockwise so that the cross section passes roughly through the middle of the cyclone and its associated wind maxima. This rotation allows for a better comparison with the normal mode cross section. However, it should be noted that a degree of longitude now corresponds to 0.87 of the unrotated value. To emphasize large scale features, the fields are averaged for 3 grid points on either side of the cross section. The vertical structure of this disturbance is similar to both that of the most unstable normal mode and of observed monsoon depressions; it has a warm over cold core structure and is strongest in the lower troposphere. However, the maximum amplitude of the warm core near 9 km is higher than that of the normal mode at 6.25 km. For comparison, composites of monsoon depressions have a warm core maximum near 7.5 km (Fig. 13 in Hunt *et al.* (2016c)), which lies midway between these two values.

Although this study is limited to the dry dynamics of monsoon depressions, perhaps one of their most standout features is the prodigious amounts of rain they can produce. This is important not only for its impact on sensible weather but also because the condensational heating produced by this precipitation has long been established as their primary energy source. Without attempting to model this aspect, we can use vertical velocity to determine where precipitation would most likely occur. The benefit of analyzing the dry wave is that we can unambiguously diagnose the adiabatic contributes to vertical velocity without the contributions from diabatic heating. Figure 11 shows the vertical velocity averaged from 1.0 to 5.0 km overlain with the winds (v') and pressure (p') at 3.2 km. It shows a pattern of ascent to the west and descent to the east. Though this region of ascent is slightly farther north than typical, this pattern is broadly similar to that of observed monsoon depressions. This distribution of vertical velocity has generally been explained using quasi-geostrophic theory (e.g.,Sanders (1984); Boos *et al.* (2015)). Perhaps the easiest way to explain it is that vorticity advection by a westward directed thermal wind would lead to ascending motion downshear, or west, of the vortex. Idealized studies of tropical-cyclone like vortices in shear yield similar patterns of vertical velocity (cite).

One of the primary benefits of linear eigenmode analyses such as presented in this study is the potential to explain the scale of the disturbance. In a standard normal mode analysis (Eq. 17), solutions of a large spectrum of wavenumbers exist, and it is generally assumed that the fastest growing normal mode dominates. By contrast, with a zonally varying basic state, solutions do not exist for arbitrary wavenumbers (Eq. 17). Instead, a preferred wavelength arises naturally. However, the wavelength and phase velocity fluctuate over the course of a wave period as the spatial structure oscillates between $A(\mathbf{r})$ and $B(\mathbf{r})$. Figure 10 shows this evolution as a function of time (Fig. 10b) along with the track of the cyclonic portion of the disturbance. Its path is labeled by day corresponding to Fig. 7 and shaded by the amplitude of its perturbation pressure. This amplitude being arbitrary, exact values are not given. The zonal wavelength is calculated by first smoothing the pressure field, finding the minimum and maximum pressure values of an adjacent trough and ridge, calculating the distance between them in the zonal direction, and then doubling this value to get a full wavelength. The gap in Fig. 10b coincides with the switch from using the ridge to the west of the cyclone to the one to the east.

Though somewhat north of average, the path of the cyclonic portion of the wave disturbance matches well with that of observed monsoon depressions, with its pressure anomaly reaching a maximum amplitude in the northern Bay of Bengal (Fig. 10a). The zonal wavelength varies from 1900 to 2600 km over the course of a full period, with an average of 2100 km. This value compares well with the 2000-2500 km wavelength of observed monsoon depressions (Sikka (1978)) and is shorter than the most unstable mode. We speculate that the length of the unstable region of the monsoon trough (2200 km) plays some role in setting this scale, though the close numerical similarity may be fortuitous. The zonal phase speed also varies, with increases in magnitude roughly corresponding to decreases in wavelength. Its average over one period is $-2.0\,\mathrm{m\,s^{-1}}$, which lies between the mean ($-1.5\,\mathrm{m\,s^{-1}}$) and mode ($-3.4\,\mathrm{m\,s^{-1}}$) of observed monsoon depressions (Boos *et al.* (2017)). This speed is somewhat slower than that of the normal mode corresponding to this wavelength, whose speed is about $3.1\,\mathrm{m\,s^{-1}}$. This discrepancy may result from the normal mode being more embedded within the easterly flow to the north. The average meridional velocity is $0.8\,\mathrm{m\,s^{-1}}$, which compares with a mean value of $1.0\,\mathrm{m\,s^{-1}}$ and mode value of $1.7\,\mathrm{m\,s^{-1}}$ for observed monsoon depressions (Boos *et al.* (2017)). Thus, in general, the phase speed of this wave is on the lower end of observed values.

The growth rates for this disturbance over a full wave period are shown in Fig. 9. For clarity, the barotropic terms (Fig. 9a) are separated from the other terms (Fig. 9b). Consistent with Eq. 17, growth rates are oscillatory. They cycle twice per wave period because energy is a quadratic quantity. Similar to the normal mode solution, the $u'v'\frac{\partial \bar{U}}{\partial y}$ term is the primary energy source. The two peaks in the growth rate correspond to the cyclone and anticyclone passing through the middle of the monsoon trough, a position which maximizes their interaction with the strong meridional shear (Fig. 7). The only other positive contributor to PKE growth is from $u'u'\frac{\partial \bar{U}}{\partial x}$, which results from the northwest-to-southeast tilt of the monsoon trough. This tilt leads to a zonal gradient of $\bar{U}$ which is acted upon by u'. All other terms in the K_e budget are small or negative. The largest energy sink comes from the artificial diffusion used to

remove small-scale waves which would otherwise dominate the solution. Considering this diffusion is likely overdone and contributes significantly to stabilizing this system, the total growth without this diffusion is also plotted in Fig. 9b. This can perhaps be considered as an upper bound on the growth rate. Even with the effect of diffusion on the growth rate removed, the net growth rate over a full wave period is negative, though it does briefly become positive. To double check, we ran experiment with the explicit diffusion set to zero and confirmed that no growing waves emerge. Another term contributing to K_e loss is the residual, which, as previously discussed, results mostly from implicit diffusion. Altogether, factors leading to this wave decaying overwhelm those leading to its growth. Such a structure could not emerge spontaneously from small-amplitude perturbations as an instability would.

5. Non-Linear Initial Value Problem (Exp. C)

We now turn to using the non-linear equation set. Since our basic state is stable and therefore cannot generate growing waves on its own, we need some initial disturbance. Considering this is one of the most convectively active regions in the world during the summer monsoon, one possible source of an initial disturbance is a vortex created by condensational heating from convection. In this experiment (Exp. C), we investigate the response of our basic state to such a heating impulse.

5.1. Experimental Design

Details of the model setup are listed in Tab. 6. Since energy dissipation is an important energy sink which substantially decreases growth rates in the linearized equations, it is useful to provide a more physically realistic calculation of its impact. No longer constrained by linearity, instead of the linear friction and artificial diffusion implemented in our previous experiments, we implement a simple turbulence closure scheme with quadratic friction. To improve the representation of topography and energy dissipation within the boundary layer, we implement a stretched grid based on Anthes (1970). The vertical grid spacing varies from 50 m at the lowest level to 1000 m at the highest level. Repeating this experiment using linear friction as in Exp. A and Exp. B without grid stretching gives similar results, though the quadratic friction decreases growth rates slightly.

5.1.1. Frictional Dissipation

This experiment uses a simplified version of the Smagorinsky scheme in WRF (cite). We set $\mathbf{s}'$ in Eq. 7a to

$$\mathbf{s}' = \frac{\partial \tau_u}{\partial z}\hat{\mathbf{i}} + \frac{\partial \tau_v}{\partial z}\hat{\mathbf{j}} \tag{18}$$

where τ_u and τ_v are the horizontal stress components induced by shear. They are defined as a time and space dependent mixing coefficient multiplied by the perturbation vertical shear.

$$\tau_u = K(\mathbf{r}, t)\frac{\partial u'}{\partial z} \tag{19a}$$

$$\tau_v = K(\mathbf{r}, t)\frac{\partial v'}{\partial z} \tag{19b}$$

The mixing coefficient K is a function of the vertical shear and static stability of the full velocity and temperature fields (i.e. basic state plus perturbation),

$$K = [l^2 C_s^2 (\frac{\partial u}{\partial z} + \frac{\partial v}{\partial z})^2 - Pr^{-1}\frac{g}{\theta}\frac{\partial \theta}{\partial z}]^{\frac{1}{2}} \tag{20}$$

where l is equal to the vertical grid spacing, $C_s = 0.25$, and $Pr = 3$.

The horizontal stress components at the surface are defined as

$$\tau_{u0} = C_D|\mathbf{v}|u \tag{21a}$$

$$\tau_{v0} = C_D|\mathbf{v}|v \tag{21b}$$

where C_D is the surface drag coefficient. We set it to 0.001 for water and 0.003 for land.

5.1.2. Heating Impulse Structure

We will represent the horizontal structure of the heating as a box oriented parallel to the monsoon trough as shown in Fig. 1. The vertical profile of this heating (Fig. 12) is based on Fig. 11 from Lin and Johnson (1996), which represents tropical oceanic convection. The magnitude of the heating is set to represent a rain rate of $6\ cm\ day^{-1}$ and is applied for 48 hours and then switched off. Applying it for a longer time period or for higher rain rates simply increases the magnitude of the resulting disturbance. The rate we have chosen produces disturbances with amplitudes comparable to those observed. Since some of the structure of the resulting disturbance comes from the heating itself independent of the basic state, we will also show results for the heating applied to a resting basic state with all basic state terms set to zero.

5.2. Results

The time evolution of the disturbance is depicted in Fig. 13, which shows the pressure (p'), wind ($\mathbf{v}'$), and basic state zonal wind ($\bar{U}$) at 48, 72, and 96 hours into the simulation at 3.1 km above sea level. The heating impulse generates a vortex which disperses into a wave and weakens with time as it moves westward. Its average motion over this time period is northwest ($300°$) at 2.8 ms^{-1}. As in Exp. B, the wavelength varies with time and longitude. For a lower bound, taking the distance between the center of the westernmost anticyclone and the cyclone as a half wavelength at day 3 yields a full wavelength of 1600 km, and taking the distance between the two anticyclones yields 2000 km. As an upper bound, taking the distance between the cyclone and easternmost anticyclone at day 4 as a half wavelength yields approximately 2500 km. These values are within the range of Exp. B (Fig. 10b) and shorter than the most unstable normal mode (Fig. 5). The same fields for the disturbance in the resting basic state are plotted in Fig. 14. By comparison, it is smaller, weaker, and does not evolve into a wave. The diameter of maximum wind is about 225 km at 72 hours, which is typical of a mesoscale convective vortex and much smaller than the disturbance in the monsoon basic state. Its velocity is north-northwestward at 1.4 ms^{-1}, which is slower than with the monsoon basic state. Since there is no background flow to advect it, this motion is best explained by the so-called "beta effect", which relies on the planetary vorticity gradient.

We now examine the vertical structure of the two disturbances in terms of wind and potential temperature (θ') using longitude-height cross sections (Fig. 15). As in Exp. B, the fields for the disturbance in the monsoon basic state are rotated $30°$ counterclockwise so that the cross section passes roughly through the middle of the cyclone and westernmost anticyclone. The cross section for the resting basic state also passes through the cyclone center but is not rotated. To emphasize the broader scale circulation features, the fields are averaged over 150 km on either side of the cross section. Results for the monsoon basic state are shown in Fig. 15a and for the resting basic state in Fig. 15b. Because the disturbance in the resting state has much more amplitude in the upper troposphere, its height scale is expanded relative to that in the monsoon basic state.

The vertical structure of the disturbance in the monsoon basic state has a warm over cold core structure with a wind maximum near 3 km. This pattern is broadly similar to that of the previous experiments (Fig. 4b and Fig. 8), though the warm core is centered about 3 km lower compared to the disturbance in the linearized zonally varying basic state. The disturbance in the resting basic state is notably different. In contrast with the disturbance in the monsoon basic state, it has a wind maximum in the upper troposphere associated with anticyclonic flow induced by the negative vertical gradient of heating aloft. Apparently, the strong easterly shear associated with the tropical easterly jet prevents disturbances from extending above the mid-troposphere. However, similar to in the monsoon basic state, it exhibits a warm over cold core structure, though is much weaker. This suggests that the structure created by the heating profile constructively interferes with and excites waves modes in this basic state. The fact that the imposed heating profile (Fig. 12) has no cooling at low levels suggests that the cold core can be at least partially attributed to cooling by ascent forced by frictional convergence near the vortex center.

Once again, it is useful to examine vertical velocity to diagnose where precipitation would be most likely be concentrated. Figure 16 shows the vertical velocity averaged from 1.0 to 5.0 km overlain with the winds (v') and pressure (p') at 3.2 km. Similar to Exp. B, ascent occurs to the west and descent to the east. However, the ascent is now concentrated more toward the southwest, in better agreement with observations. All of this is consistent with the rainfall in monsoon depressions being heavily biased toward the southwest corner of their circulation.

Once again, we present an energy budget based on Eq. 14. We include both a time series of the mass-weighted average of various terms in the budget (Fig. 17a) and of the growth rates (Fig. 17b). To simplify the analysis, we note that some of the barotropic terms represent essentially the same process rotated $90°$ and can be grouped together. We will call these new combined terms the horizontal shear term ($u'v'\frac{\partial \bar{U}}{\partial y} + u'v'\frac{\partial \bar{V}}{\partial x}$), the horizontal convergence term ($u'^2\frac{\partial \bar{U}}{\partial x} + v'^2\frac{\partial \bar{V}}{\partial y}$), and the vertical shear term ($u'w'\frac{\partial \bar{U}}{\partial z} + v'w'\frac{\partial \bar{V}}{\partial z}$).

Because the heating source is switched off after 48 hours, it is best to consider the periods before and after this time separately. During the first 48 hours, while the heating is being applied, the largest term is pressure work. This is a reflection of the drop in hydrostatic pressure caused by the heating which in turn accelerates the perturbation wind. The second largest source of K_e is associated with the vertical shear. This energy comes primarily from the vertical velocity induced by the heating transporting eastward momentum upward. Recall that neither of these two terms were significant sources of K_e in the normal mode (Fig. 5); both result from the interaction of the imposed heating with the basic state. While the heating is being applied, K_e generation from horizontal shear and horizontal convergence also increase. In addition to these K_e sources, friction, advection, and the residual serve as energy sinks. In this case, the residual most likely results from numerical diffusion implicit in the 5th-order advection scheme.

After the heating is switched off, the energetics more closely resemble that of Exp. A and B. Without the vertical velocity and hydrostatic pressure falls forced by the heating, the vertical shear and pressure work terms become negative. By contrast, the horizontal shear term emerges as the largest source of K_e with only minor contributions from horizontal convergence. However, similar to Exp. B, it is not undergoing unstable growth. Although its growth rate from horizontal shear is similar to that of the most unstable normal mode at $0.5x?day^{-1}$, the energy sources approximately balance the energy sinks. This balance leads to several days of near steady K_e with a slow decline afterward. Nevertheless, even if stable, this disturbance still draws substantial amounts of energy from the basic state shear.

5.3. Sensitivity to Heating Location

Although reasonable increases in the size and amplitude of the heating impulse results simply in a larger amplitude disturbance, the sensitivity of the response to its location is much more interesting. To explore this, Exp. C is repeated by applying the heating region at every point on a 200 km by 200 km grid within a rectangle bounded to the south and north by latitudes $11.3°$N and $27.5°$N and to the west and east by $70.7°$E and $105.7°$E. This layout results in 200 different experiments. To summarize these experiments, we calculate the total amount of K_e produced by various physical process by integrating the rate of K_e generation for selected terms in Eq. 14. These values are then plotted on a map at the center of each heating parallelogram. We will split our analysis into two time periods: one limited to the first 48 hours of the simulation, during which the heating is being applied (Fig. 18), and one from 51 to 144 hours, during which the heating has been switched off (Fig. 19).

During the first 48 hours of simulation, K_e production is dominated by the pressure work and vertical shear terms throughout many of the experiments (Fig. 18). As the vertical shear term reflects upward momentum transport by the vertical velocity induced by the heating, it is highest to the southwest where the basic state vertical shear is largest. However, on closer inspection, this extra K_e does not ultimately lead to stronger vortices; it is more indicative of the disturbance being sheared apart and hence is probably not an important energy source for monsoon depressions. What does appear important, however, is the pressure work term, which is maximized when heating is applied within the monsoon trough. This pattern can perhaps best be explained by understanding how the basic state affects the deformation radius, defined as

$$L_R = \frac{NH}{\bar{\zeta} + \zeta' + f} \tag{22}$$

where N is the Brunt-Vaisala frequency, H is the depth scale, $\bar{\zeta}$ and ζ' are the basic state and perturbation relative vorticity, and f is the planetary vorticity. Where the deformation radius is small, temperature perturbations generated by heating are more efficiently converted to perturbation kinetic energy associated with balanced flow. Within the monsoon trough, L_R is small because $\bar{\zeta}$ is maximized and f is larger due to its more northerly location within the domain. Additionally, because a vortex forming within the weaker vertical shear of the monsoon trough will not be sheared apart as quickly, and the increasing perturbation vorticity (ζ') will further decrease L_R. An equivalent explanation is that the rate of vorticity production by vertical stretching will be highest where the absolute vorticity (i.e. $\bar{\zeta} + \zeta' + f$) is largest. Taken alone, this analysis may appear to suggest that vortex formation frequency—and by extension, monsoon depression frequency—from convective heating is nearly uniform along the monsoon trough axis with a maximum in the northwest. However, it should be noted that, although the heating rates in our experiments are held constant, precipitation is climatologically much higher toward the southeastern end of the monsoon trough. Including this factor would presumably shift the maximum more toward the Bay of Bengal, where observed monsoon depression frequency is highest.

After 48 hours, the heating is switched off and the disturbance freely evolves within the basic state flow (Fig. 19). In contrast with the previous 48 hours, K_e growth from horizontal shear is by far the dominant term. This growth is concentrated in two regions: one in the northernmost Bay of Bengal and adjacent land areas and one in the northwestern monsoon trough. The former coincides closely with the observed maximum track density of monsoon depressions (Fig. 6a in Hurley and Boos (2015)) and suggests that convection forming in the northernmost Bay of Bengal is especially favorable for monsoon depression formation. It is localized because the basic state shear becomes increasing stable to the east (Fig. 6) and disturbances forming to the northwest are quickly advected out of the region of highest meridional shear. The second maximum in energy conversion, however, lies in a region of much lower track density. As it is colocated with a region of increased pressure work (Fig. 19d), disturbances in this region may grow from both baroclinic and barotropic processes. This is consistent with Fig. 6 from Exp. A.

6. Discussion and Conclusions

Though far from complete, this set of idealized experiments provides a potential starting point for understanding the basic dynamics of monsoon depressions. To the extent that they can be explained by linear instability theory, our results suggest that barotropic instability is most relevant. In the simplest case of a zonally symmetric basic state, it yields a most unstable normal mode which reproduces many of the observed features of monsoon depressions, including their warm over cold core structure, low-level wind maximum, and slow, westward propagation. However, given that these modes are similar in length to the region of the monsoon trough which can support barotropic instability, the zonally varying basic state is perhaps more relevant. In this case, a linear instability analysis reveals wave modes whose structure and energetics closely resemble that of the normal mode solutions, but which decay with time as barotropic energy conversion is unable to overcome energy lost through dissipative processes. The 2200 km wavelength of this mode is shorter than the most unstable normal mode and in close agreement with observed monsoon depressions. Although such a decaying mode would not develop spontaneously, it can be forced by applying a localized heating impulse within the monsoon trough with a vertical profile representative of oceanic moist convection. Additionally, consistent with recent work (Cohen and Boos (2016)), we find no baroclinic instability. In fact, in most of our simulations, the opposite occurs: perturbation kinetic energy is transformed into potential energy associated with temperature perturbations through the pressure work term. Of course, this experiment alone cannot dismiss the possibility of moist baroclinic instability as the impact of condensational heating from precipitation is not simulated.

As discussed in the introduction, support for barotropic instability in past literature is mixed. Some studies find significant disagreement between the structure of barotropic instabilities and observed monsoon depressions while others find that barotropic energy conversion is insignificant to their energetics. Here we address some of these issues. The main studies which have successfully isolated barotropically unstable modes in the mid-tropospheric flow find disturbances whose phase velocity is in the wrong direction Nitta and Masuda (1981); Subrahmanyam et al. (1981). This could be a consequence of them neglecting the large vertical variations in the basic state flow. Even though barotropic instability is at its simplest a two-dimensional phenomenon, these variations may be important for the phase velocity. On the other hand, those studies finding unstable normal modes in the upper troposphere (Shukla 1978; Goswami et al. 1980) are partially consistent with our results; in order to isolate lower-tropospheric modes with wavelengths longer than about 3500 km, we had to damp the faster growing upper-tropospheric modes. Our results suggest that these upper-tropospheric waves are artifacts of the zonal symmetry, since they do not appear in the zonally varying basic state. Of course, some of the discrepancies may stem from the particular choice of basic state. This is somewhat more difficult to assess.

A seemingly more significant problem is that our results appear to run contrary to a number of observational studies which come to the opposite conclusion: energy is transferred from the perturbation flow associated with monsoon depressions to the larger-scale monsoon trough (Rajamani 1985; Rajamani and Sikdar 1989; Krishnamurti et al. 2013). However, this disagreement probably results from the different methods used to assess this transfer. Whereas we calculate transfer between a perturbation and a time-independent basic state, previous studies have used a zonal-mean eddy decomposition (Lorenz 1967). There are a number of problems with this latter approach. First, although it is valid only for a global domain, these studies apply it over a domain limited to the monsoon region. Therefore, any conclusions from such an analysis should be approached with caution. Second, since the monsoon trough itself exhibits large deviations from the zonal mean, its energetics would contribute a significant portion to the eddy flow. Consequently, such a

decomposition would not properly separate the monsoon depressions from the monsoon trough. In fact, with its northwest-to-southeast orientation, the monsoon trough tilts downshear relative to the zonal mean flow, a configuration which would contribute negatively to the barotropic energy conversion term and potentially overwhelm any positive contribution from an upshear tilted monsoon depression. Finally, the zonal-mean or time-mean eddy decomposition traditionally used in observational studies would yield slightly different results compared with idealized modeling studies which use a time-independent basic state. For barotropic instability, this averaging would reduce the meridional shear.

Though not the main focus of this study, our experiments can contribute some value to the discussion of why monsoon depressions move northwestward, a topic which has received considerable attention over the years due to their apparent propagation against the westerly monsoon flow. A key result is that all of the wave modes we have isolated have a westward or northwestward phase velocity. To the extent that they can describe monsoon depressions, it supports the hypothesis that the direction of propagation can be explained by adiabatic dynamics alone (Boos *et al.* 2015). As such, our results are inconsistent with the argument that vortex stretching by convection is necessary for their westward propagation (Daggupaty and Sikka 1977; Chen *et al.* 2005; Adames and Ming 2018b). Nevertheless, in the real atmosphere, a variety of mechanisms likely contribute to their overall motion, including the impact of moist convection, interaction with the Himalayas (Hunt and Parker 2016), or non-linear advection (Boos *et al.* 2015). Indeed, as the phase velocities in our experiments are somewhat slower than typically observed, it is possible that one or more of these processes could make up for the difference.

Regardless of how closely the resulting wave modes may resemble monsoon depressions, several deficiencies make the growth mechanism presented in this study an incomplete explanation of their origin and amplification. Firstly, since the net growth rates are negative for the zonally varying basic states, such structures could not emerge spontaneously from small, random perturbations as in traditional instability theories. We can provide some speculation on ways to resolve this issue. One possibility is that the monsoon trough briefly reaches a state of barotropic instability before being stabilized by the growing disturbance. Although our technique to construct a representative basic state aimed to retain the strong meridional shear, perhaps an even shorter averaging period would lead to a barotropically unstable basic state. On the other hand, if instability is rare, an initial disturbance of sufficient amplitude is needed. It has been well documented that monsoon depressions often have upstream predecessors, such easterly waves or typhoons from the western Pacific (Chen and Weng 1999). The increased shear in the monsoon trough could allow these disturbances to reamplify. Nevertheless, they are often observed to develop *in situ*, with no apparent precursor. The results from Exp. C suggest that, even for a stable basic state, convection concentrated in the Bay of Bengal can generate a vortex which projects onto the linear wave mode isolated in Exp. B. Although its net growth rate is near zero, it still extracts energy from the background meridional shear. Though we have no proof that such a process occurs in nature, considering that the eastern Bay of Bengal is one of the most convectively active regions in the world during summer, it is at least plausible. This argument is very similar to some hypotheses on the origin of African easterly waves (Hall *et al.* 2006; Thorncroft *et al.* 2008). The monsoon trough may be particularly favorable because of the high inertial stability which leads to efficient conversion of diabatic heating to kinetic energy.

A separate but related problem is that, even if one of the mechanisms listed above can produce a disturbance, how does it continue to grow? This is where we speculate that condensational heating from precipitation is important. The structures generated in our experiments have a relatively deep, concentrated region of ascent to the west and southwest of the cyclonic vortex. Because it exists independent of buoyant accelerations caused by moist convection, it can organize precipitation whose condensational heating can generate kinetic energy which feeds back onto the circulation. This scenario would give a role for the vertical shear: a vortex growing through horizontal shear and interacting with vertical shear produces strong vertical velocity which can organize precipitation. Most other studies of their energetics have established diabatic heating by cumulus convection as their primary energy source. We argue that the wave modes isolated in our experiments provide the organizing structure needed for monsoon depressions amplification, even if condensational heating is a larger source of energy. After all, cumulus convection may be ubiquitous, but monsoon depressions are not.

References

Adames ÁF, Ming Y. 2018a. Interactions between water vapor and potential vorticity in synoptic-scale monsoonal disturbances: Moisture vortex instability. *Journal of the Atmospheric Sciences* (2018).

Adames ÁF, Ming Y. 2018b. Moisture and moist static energy budgets of south asian monsoon low pressure systems in gfdl am4. 0. *Journal of the Atmospheric Sciences* (2018).

Anthes RA. 1970. Numerical experiments with a two-dimensional horizontal variable grid. *Monthly Weather Review* **98**(11): 810–822.

Arndt DS, Basara JB, McPherson RA, Illston BG, McManus GD, Demko DB. 2009. Observations of the overland reintensification of tropical storm erin (2007). *Bulletin of the American Meteorological Society* **90**(8): 1079–1093.

Bannon PR. 1995. Potential vorticity conservation, hydrostatic adjustment, and the anelastic approximation. *Journal of the atmospheric sciences* **52**(12): 2302–2312.

Boos W, Hurley J, Murthy V. 2015. Adiabatic westward drift of indian monsoon depressions. *Quarterly Journal of the Royal Meteorological Society* **141**(689): 1035–1048.

Boos WR, Mapes BE, Murthy VS. 2017. Potential vorticity structure and propagation mechanism of indian monsoon depressions. In: *The Global Monsoon System: Research and Forecast*, World Scientific, pp. 187–199.

Chen TC, Weng SP. 1999. Interannual and intraseasonal variations in monsoon depressions and their westward-propagating predecessors. *Monthly weather review* **127**(6): 1005–1020.

Chen TC, Yoon JH, Wang SY. 2005. Westward propagation of the indian monsoon depression. *Tellus A* **57**(5): 758–769.

Chorin AJ. 1968. Numerical solution of the navier-stokes equations. *Mathematics of computation* **22**(104): 745–762.

Cohen NY, Boos WR. 2016. Perspectives on moist baroclinic instability: implications for the growth of monsoon depressions. *Journal of the Atmospheric Sciences* **73**(4): 1767–1788.

Daggupaty SM, Sikka DR. 1977. On the vorticity budget and vertical velocity distribution associated with the life cycle of a monsoon depression. *Journal of the Atmospheric Sciences* **34**(5): 773–792.

Dee DP, Uppala S, Simmons A, Berrisford P, Poli P, Kobayashi S, Andrae U, Balmaseda M, Balsamo G, Bauer P, *et al.* 2011. The era-interim reanalysis: Configuration and performance of the data assimilation system. *Quarterly Journal of the royal meteorological society* **137**(656): 553–597.

Ditchek SD, Boos WR, Camargo SJ, Tippett MK. 2016. A genesis index for monsoon disturbances. *Journal of Climate* **29**(14): 5189–5203.

Emanuel KA. 1986. An air-sea interaction theory for tropical cyclones. part i: Steady-state maintenance. *Journal of the Atmospheric Sciences* **43**(6): 585–605.

Goswami B, Keshavamurty R, Satyan V. 1980. Role of barotropic, baroclinic and combined barotropic-baroclinic instability for the growth of monsoon depressions and mid-tropospheric cyclones. *Proceedings of the Indian Academy of Sciences-Earth and Planetary Sciences* **89**(1): 79–97.

Hall NM, Kiladis GN, Thorncroft CD. 2006. Three-dimensional structure and dynamics of african easterly waves. part ii: Dynamical modes. *Journal of the Atmospheric Sciences* **63**(9): 2231–2245.

Hall NM, Sardeshmukh PD. 1998. Is the time-mean northern hemisphere flow baroclinically unstable? *Journal of the atmospheric sciences* **55**(1): 41–56.

Hunt KM, Parker DJ. 2016. The movement of indian monsoon depressions by interaction with image vortices near the himalayan wall. *Quarterly Journal of the Royal Meteorological Society* **142**(698): 2224–2229.

Hunt KM, Turner AG, Inness PM, Parker DE, Levine RC. 2016a. On the structure and dynamics of indian monsoon depressions. *Monthly Weather Review* **144**(9): 3391–3416.

Hunt KM, Turner AG, Parker DE. 2016b. The spatiotemporal structure of precipitation in indian monsoon depressions. *Quarterly Journal of the Royal Meteorological Society* **142**(701): 3195–3210.

Hunt KM, Turner AG, Parker DE. 2016c. The spatiotemporal structure of precipitation in indian monsoon depressions. *Quarterly Journal of the Royal Meteorological Society* **142**(701): 3195–3210.

Hurley JV, Boos WR. 2015. A global climatology of monsoon low-pressure systems. *Quarterly Journal of the Royal Meteorological Society* **141**(689): 1049–1064.

Kasture S, Keshavamurty R, Satyan V. 1993. A model study of the growth of summer monsoon disturbances. *Current Science* : 673–679.

Krishnakumar V, Keshavamurty R, Kasture S. 1992. Moist baroclinic instability and the growth of monsoon depressionslinear and nonlinear studies. *Proceedings of the Indian Academy of Sciences-Earth and Planetary Sciences* **101**(2): 123–152.

Krishnamurti T, Kanamitsu M, Godbole R, Chang CB, Carr F, Chow JH. 1976. Study of a monsoon depression (ii), dynamical structure. *Journal of the Meteorological Society of Japan. Ser. II* **54**(4): 208–225.

Krishnamurti T, Martin A, Krishnamurti R, Simon A, Thomas A, Kumar V. 2013. Impacts of enhanced ccn on the organization of convection and recent reduced counts of monsoon depressions. *Climate dynamics* **41**(1): 117–134.

Krishnamurti T, Molinari J, Pan Hl, Wong V. 1977. Downstream amplification and formation of monsoon disturbances. *Monthly Weather Review* **105**(10): 1281–1297.

Lin X, Johnson RH. 1996. Heating, moistening, and rainfall over the western pacific warm pool during toga coare. *Journal of the atmospheric sciences* **53**(22): 3367–3383.

Lindzen R, Farrell B, Rosenthal A. 1983. Absolute barotropic instability and monsoon depressions. *Journal of the Atmospheric Sciences* **40**(5): 1178–1184.

Lorenz E. 1967. *The nature and theory of the general circulation of the atmosphere*, vol. 218. World Meteorological Organization Geneva.

Mishra S. 2018. On the evolution of planetary-scale fields and genesis of monsoon depressions over the indian region. *Quarterly Journal of the Royal Meteorological Society* **144**(710): 129–141.

Mishra S, Salvekar P. 1980. Role of baroclinic instability in the development of monsoon disturbances. *Journal of the Atmospheric Sciences* **37**(2): 383–394.

Montgomery MT, Smith RK. 2014. Paradigms for tropical cyclone intensification. Technical report, NAVAL POSTGRADUATE SCHOOL MONTEREY CA DEPT OF METEOROLOGY.

Moorthi S, Arakawa A. 1985. Baroclinic instability with cumulus heating. *J. Atmos. Sci.* **42**(19): 2007–2031.

Nagar S, Bawiskar S, Chinthalu G, Kulkarni J. 2009. Study of dynamical structure of an unusual monsoon depression formed over the bay of bengal during august 2006. *Pure and applied geophysics* **166**(3): 485–507.

Nitta T, Masuda K. 1981. bservational study of a monsoon depression developed over the bay of bengal during summer monex. *Journal of the Meteorological Society of Japan. Ser. II* **59**(5): 672–682.

Orlanski I, Chang EK. 1993. Ageostrophic geopotential fluxes in downstream and upstream development of baroclinic waves. *Journal of the atmospheric sciences* **50**(2): 212–225.

Rajamani S. 1985. Energetics of the monsoon circulation over south asia. ii. energy terms and energy transformation terms. *Mausam* **36**: 405–412.

Rajamani S, Sikdar D. 1989. Some dynamical characteristics and thermal structure of monsoon depressions over the bay of bengal. *Tellus A: Dynamic Meteorology and Oceanography* **41**(3): 255–269.

Rao VB. 1971. Dynamic instability of the zonal current during a break monsoon. *Tellus* **23**(1): 111–112.

Saha K, Chang C. 1983. The baroclinic processes of monsoon depressions. *Monthly weather review* **111**(7): 1506–1514.

Saha K, Sanders F, Shukla J. 1981. Westward propagating predecessors of monsoon depressions. *Monthly Weather Review* **109**(2): 330–343.

Salvekar P, George L, Mishra S. 1986. Low level wind shear and baroclinic growth of monsoon depression scale waves. *Meteorology and Atmospheric Physics* **35**(1-2): 10–18.

Salvekar P, Mishra S. 1985. Baroclinic energetics and zonal plane distribution of monsoon disturbances. *pure and applied geophysics* **123**(3): 448–462.

Sanders F. 1984. Quasi-geostrophic diagnosis of the monsoon depression of 5–8 july 1979. *Journal of the Atmospheric Sciences* **41**(4): 538–552.

Shukla J. 1977. Barotropic-baroclinic instability of mean zonal wind during summer monsoon. *pure and applied geophysics* **115**(5-6): 1449–1461.

Shukla J. 1978. Cisk-barotropic-baroclinic instability and the growth of monsoon depressions. *Journal of the Atmospheric Sciences* **35**(3): 495–508.

Sikka D. 1978. Some aspects of the life history, structure and movement of monsoon depressions. In: *Monsoon Dynamics*, Springer, pp. 1501–1529.

Simmons A, Wallace J, Branstator G. 1983. Barotropic wave propagation and instability, and atmospheric teleconnection patterns. *Journal of the Atmospheric Sciences* **40**(6): 1363–1392.

Subrahmanyam D, Tandon M, George L, Mishra S. 1981. Role of barotropic mechanism in the development of a monsoon depression: A monex study. *pure and applied geophysics* **119**(5): 901–912.

Thorncroft CD, Hall NM, Kiladis GN. 2008. Three-dimensional structure and dynamics of african easterly waves. part iii: Genesis. *Journal of the Atmospheric Sciences* **65**(11): 3596–3607.

Wicker LJ, Skamarock WC. 2002. Time-splitting methods for elastic models using forward time schemes. *Monthly weather review* **130**(8): 2088–2097.

Table 1. Model Parameters

	Experiment A	Experiment B	Experiment C
Equation Set	Linear	Linear	Non-Linear
Horizontal Spacing ($\Delta x = \Delta y$)	100 km	75 km	50 km
Vertical Grid Spacing (Δz)	500 m	500 m	Stretched
Time Step (Δt)	600 s	450 s	300 s
Grid Points (N_x, N_y, N_z)	variable, 40, 40	95, 46, 42	140, 65, 40
Latitude Range	$1°$ - $36°$N	$3°$ - $32°$N	$6°$ - $35°$N
Longitude Range	Fixed Value	$55°$ - $120°$E	$50°$ - $115°$E
Horizontal Diffusion (α_x,α_y)	$0, 1.2 \times 10^{-3}$	$1.2 \times 10^{-2}, 1.2 \times 10^{-2}$	No explicit
Vertical Diffusion (α_z)	1.2×10^{-4}	1.2×10^{-3}	Flow based 2nd Order
Surface Friction (s_0)	2×10^{-5}	2×10^{-5}	Quadratic Drag
Boundary Width (north, south, east, west)	10, 6, periodic	5, 5, 5, 5	5, 5, 5, 5
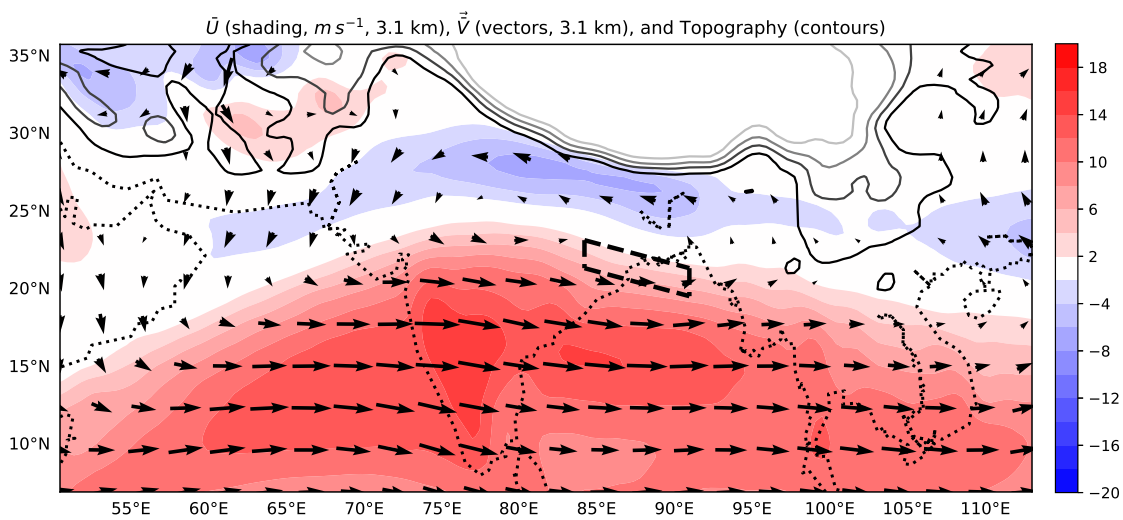
Figure 1. Basic state zonal wind ($\bar{U}$, shading, $m\ s^{-1}$, $3.1\ km$), basic state wind ($\bar{V}$, vectors, $3.1\ km$), and height of topography (contoured every $1.0 km$). Dashed box shows region where heating is applied in Exp. C.

(a) $\bar{U}$ (shading, $m\,s^{-1}$) and $\bar{\theta}$ (contours, K)

(b) Basic State Absolute Vorticity ($\bar{\zeta} + f$, $10^5\,s^{-1}$)
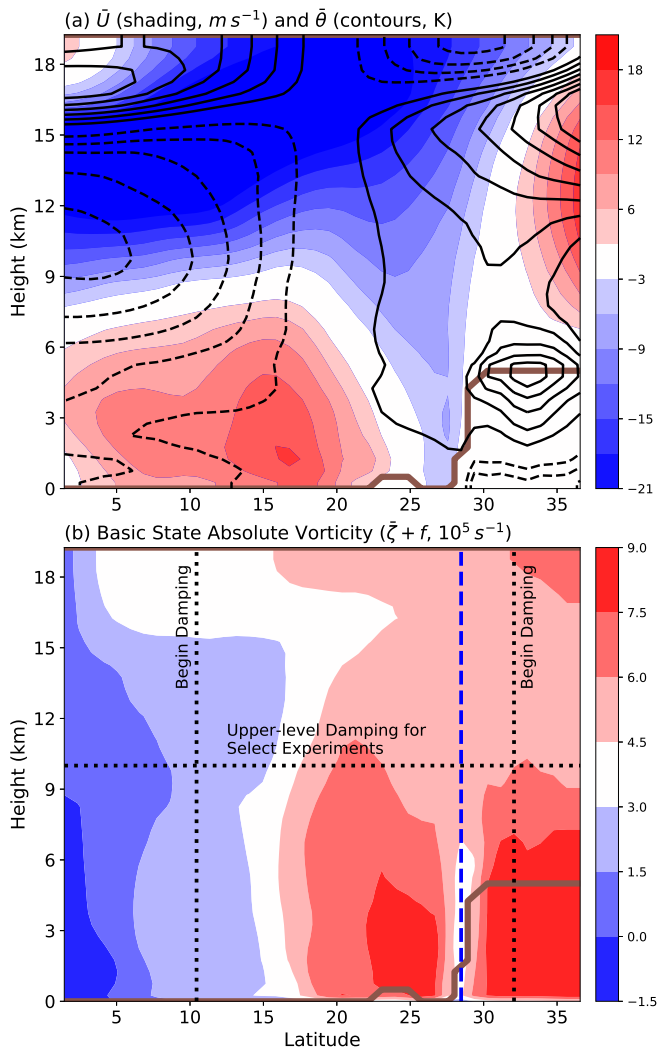
Figure 2. Latitude-height cross section at $87°$E of the (a) basic state zonal winds ($\bar{U}$, shading, $m\,s^{-1}$) and basic state potential temperature ($\bar{\theta}$, contoured every 1.3 K) and (b) basic state absolute vorticity ($\bar{\zeta} + f$, shading, s^{-1}). The topography is outlined in brown in both plots. The dotted black lines in (b) show the location of the boundary conditions used for some of the experiments in Exp. A. The dashed blue line shows the location north of which the basic state fields are set to a constant in Exp. A.

p' (shading, hPa, 3.25 km), $\vec{v}'$ (vectors, 3.25 km), w' (contours, 1-5 km average)
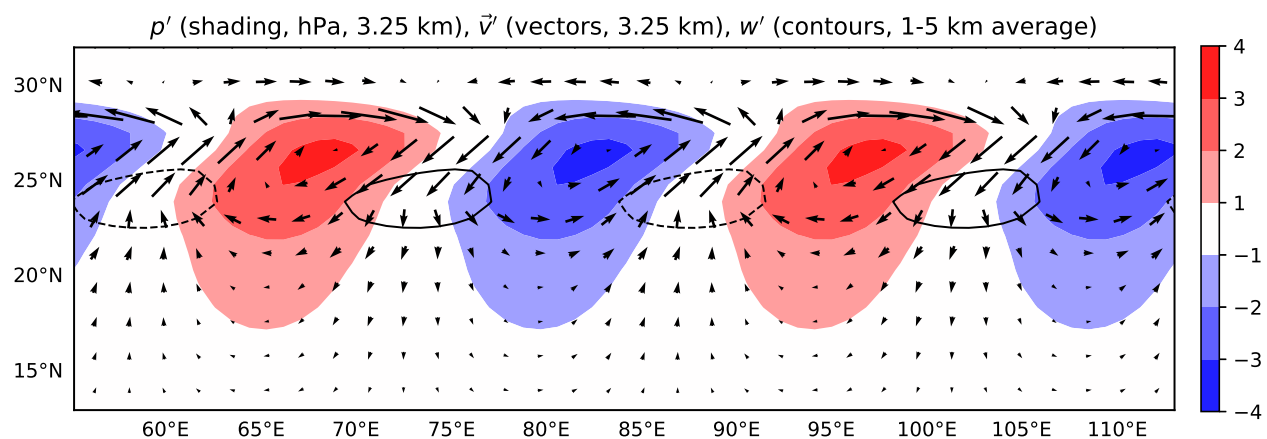
Figure 3. Perturbation pressure (p', shading, hPa, $3.25\ km$), perturbation winds ($\mathbf{v}'$, vectors, $3.25\ km$), and perturbation vertical velocity (w', contoured every $0.3\ cm\ s^{-1}$, averaged from $1.0\ km$ to $5.0\ km$) for the $3200\ km$ wavelength normal mode.
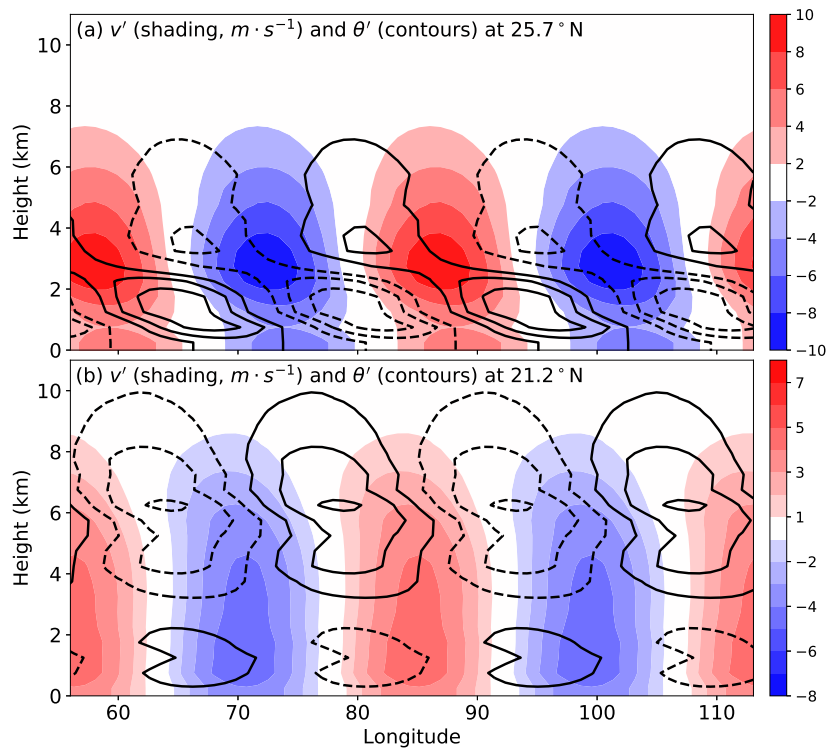
Figure 4. Longitude-height cross section at (a) $25.7°$N and (b) $21.2°$N of perturbation wind (v', shading, ms^{-1}) and perturbation potential temperature ($θ'$, contoured every 1.6 K for (a) and 0.63 K for (b)) for the 3200 km wavelength normal mode. Note the change in the shading scale for the wind.
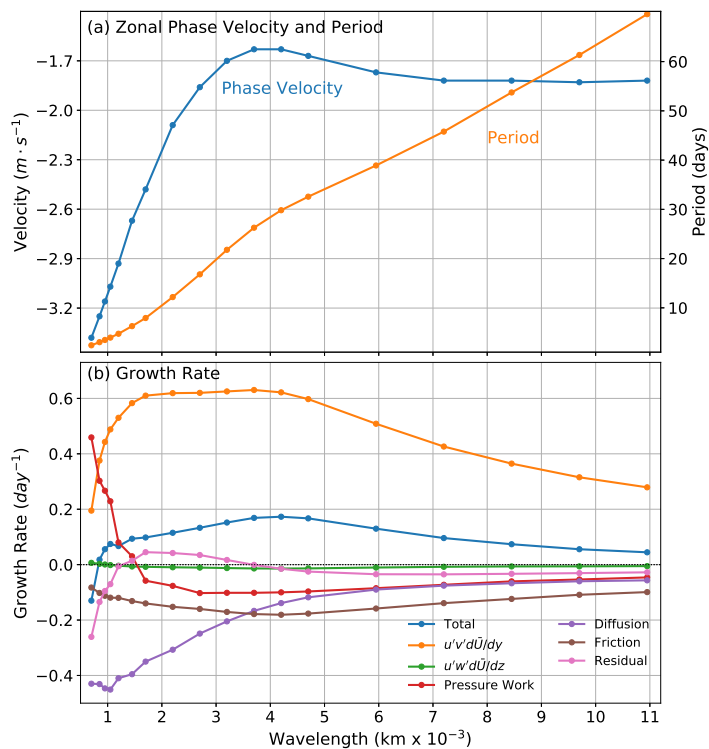
Figure 5. As a function of wavelength, (a) Zonal phase velocity and period and (b) growth rates for indiviual terms in Eq. 14 for Exp. A. Each individual experiment used to construct this relationship is marked by a dot.
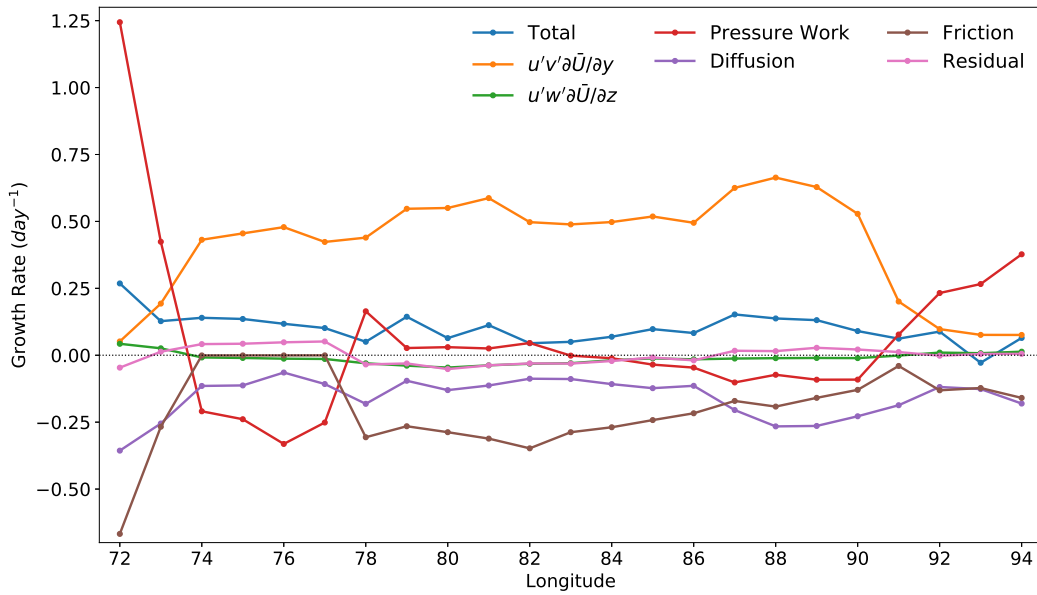
Figure 6. Growth rates as a function of longitude for indiviual terms in Eq. 14 for Exp. A. Each individual experiment used to construct this relationship is marked by a dot.
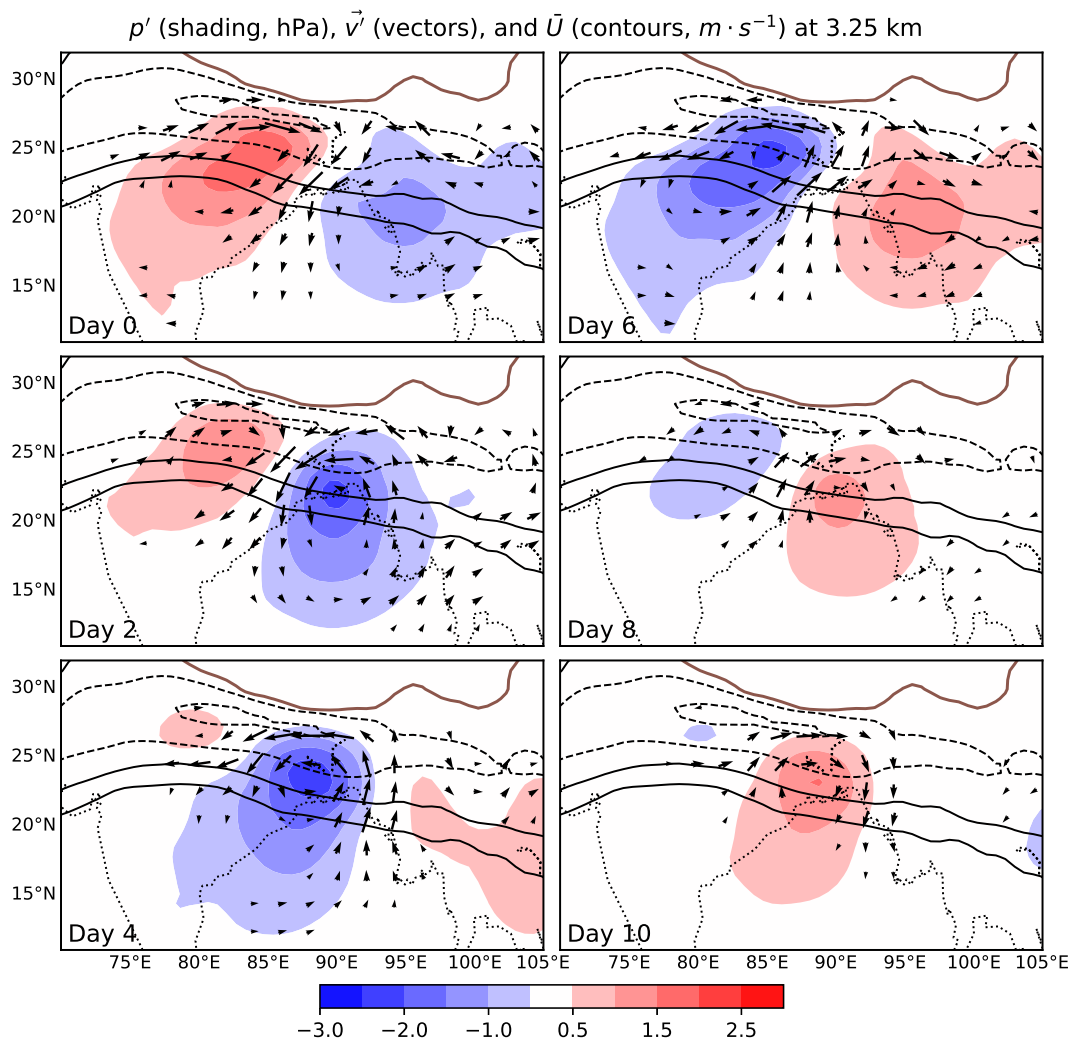
Figure 7. Time evolution of perturbation pressure (p', shading, hPa, 3.25 km), perturbation winds ($\mathbf{v}'$, vectors, 3.25 km), and basic state zonal wind ($\bar{U}$, contoured every 4 ms^{-1}) between -6 ms^{-1} and 6 ms^{-1}, 3.25 km) for Exp. B
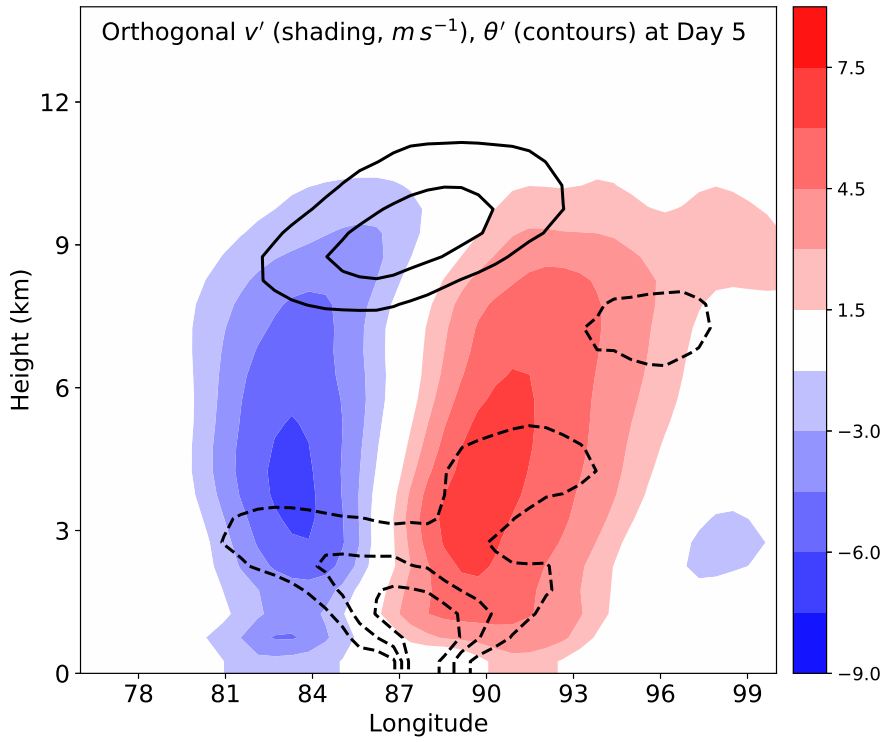
Figure 8. Longitude-height cross section of the component of perturbation wind orthogonal to the cross section (shading, $m\,s^{-1}$) and perturbation potential temperature (θ', contoured every 1 K excluding zero contour) at day 5. This cross section is rotated $30°$ clockwise from a line of constant longitude and the fields are averaged for 225 km on either side of the cross section. Because of this rotation, longitude on the x-axis corresponds to 0.87 of its normal length.
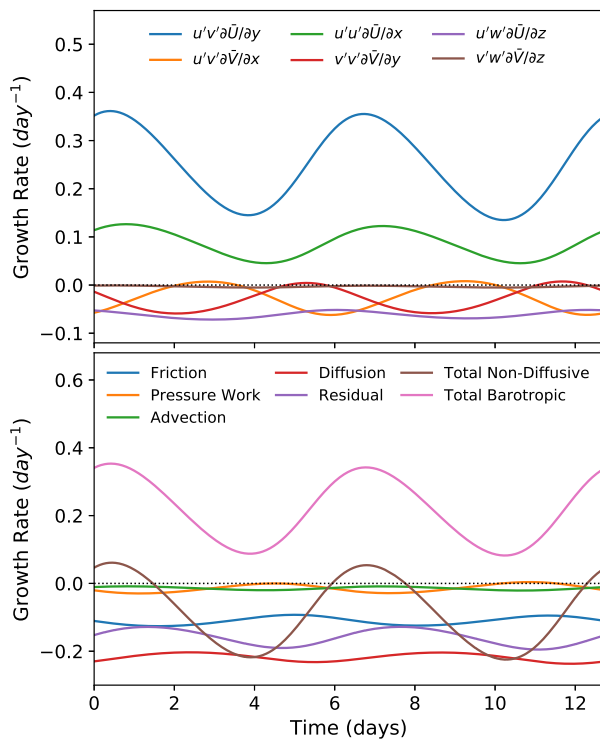
Figure 9. Growth rate as a function of time with dates corresponding to Fig. 7
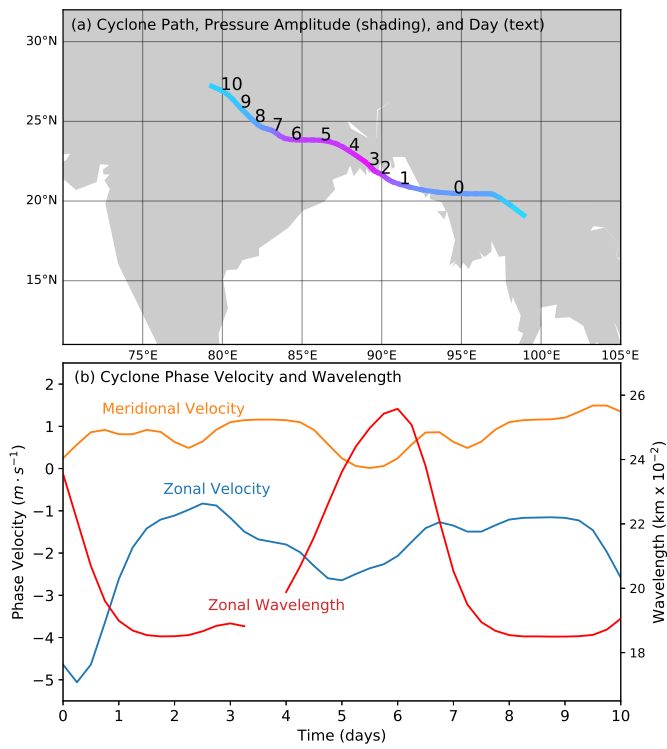
Figure 10. (a) Track of the center of the cyclonic phase of the wave disturbance shaded by magnitude of pressure perturbation and overlaid with dates corresponding to Fig. 7 and (b) zonal and meridional phase velocity and zonal wavelength as a function of time.
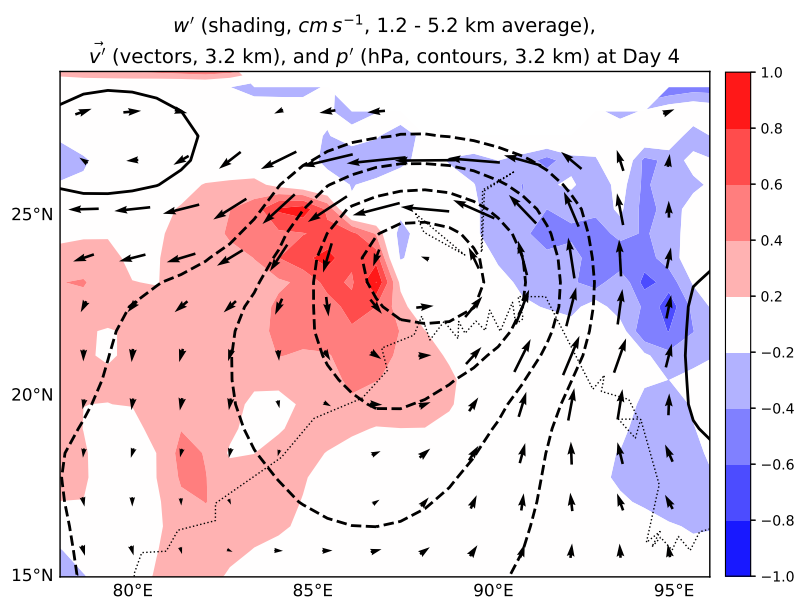

Figure 11. Perturbation vertical velocity (w', shading, $cm\,s^{-1}$, averaged from 1.0 to 5.0 km) and perturbation winds ($\mathbf{v}'$, vectors, 3.25 km) at day 4.
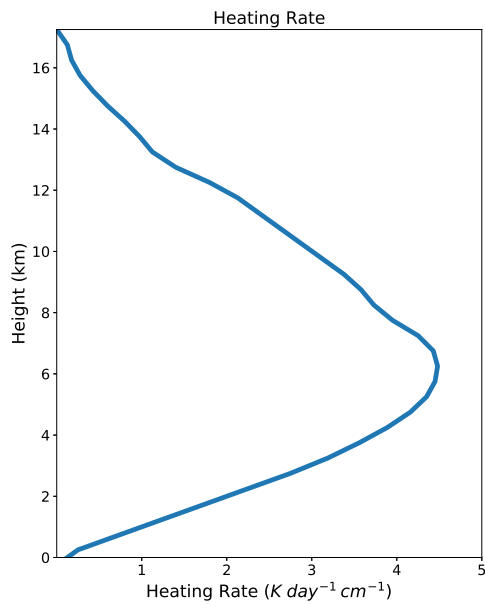
Figure 12. Profile of heating rate normalized by precipitation rate (s_θ,K).
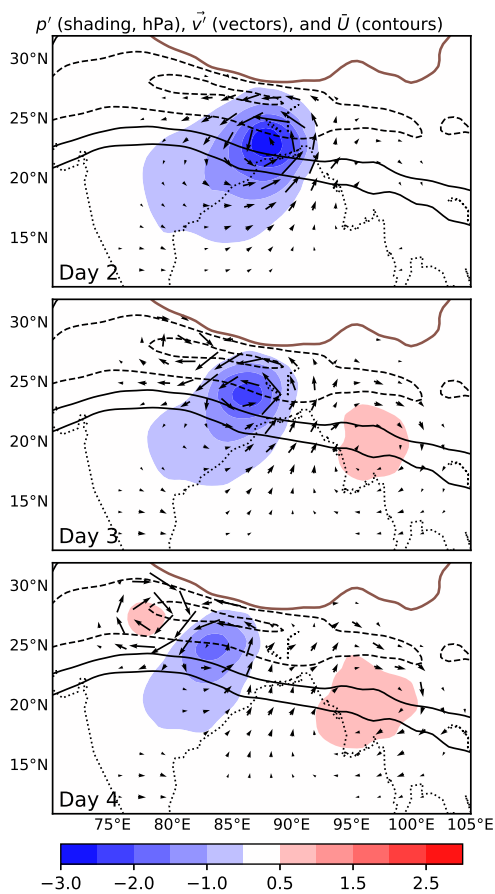

Figure 13. Perturbation pressure (p', shading, hPa, 3.1 km), perturbation winds ($\mathbf{v}'$, vectors, 3.1 km), and basic state zonal wind ($\bar{U}$, contoured every 4 ms^{-1}) between -6 ms^{-1} and 6 ms^{-1}) for hours 48, 72, and 96 into the simulation with a basic state representative of the monsoon region.
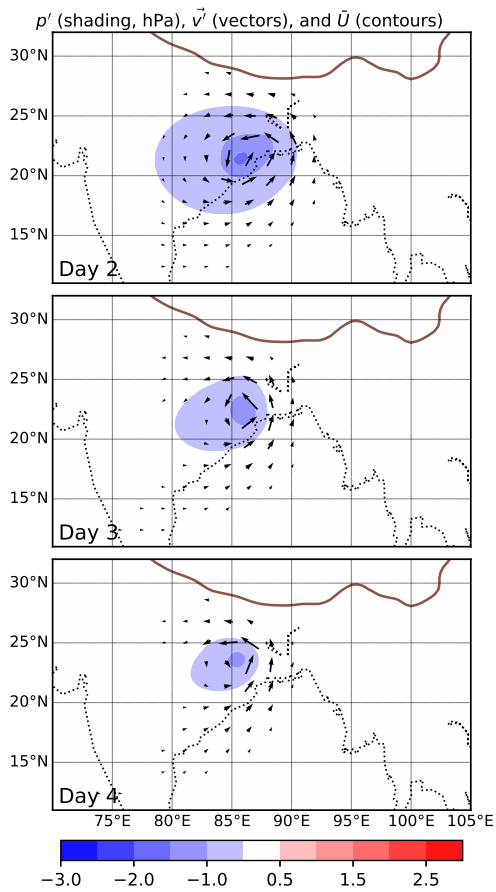
p' (shading, hPa), $\vec{v}'$ (vectors), and $\bar{U}$ (contours)

Day 2

Day 3

Day 4

Figure 14. As in Fig. 13, but with the resting basic state.

Orthogonal v' (shading, $m\,s^{-1}$), θ' (contours) at Day 3

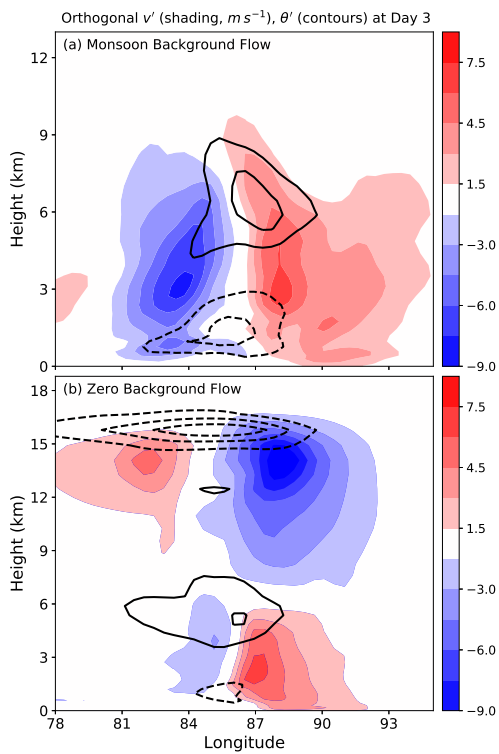(a) Monsoon Background Flow

(b) Zero Background Flow

Figure 15. Longitude-height cross section of component of perturbation wind orthogonal to cross section (shading, $m\,s^{-1}$) and perturbation potential temperature (θ', K, contours) at 72 hours into the simulation for (a) monsoon basic state and (b) resting basic state. Note the change in the y-axis scale.
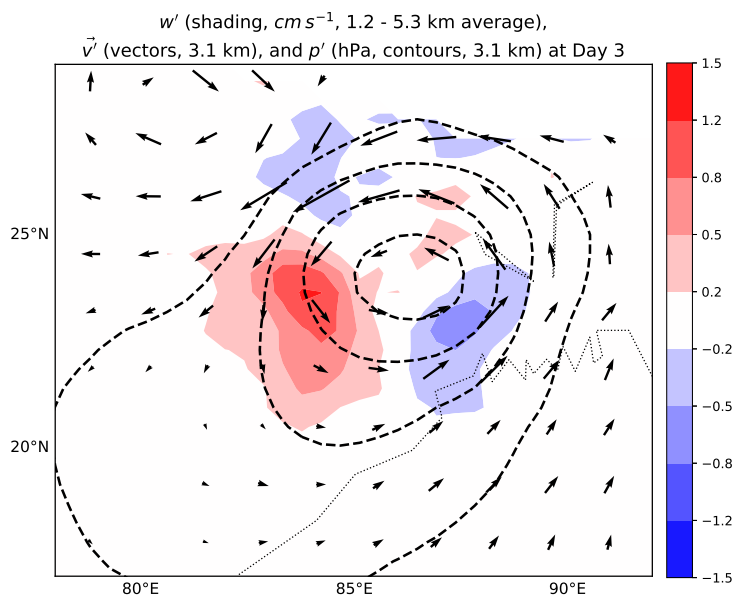
Figure 16. Perturbation vertical velocity (w', shading, $cm\,s^{-1}$, averaged from 1.2 to 5.3 km) and perturbation winds ($\mathbf{v}'$, vectors, 3.1 km) at 72 hours into the simulation.
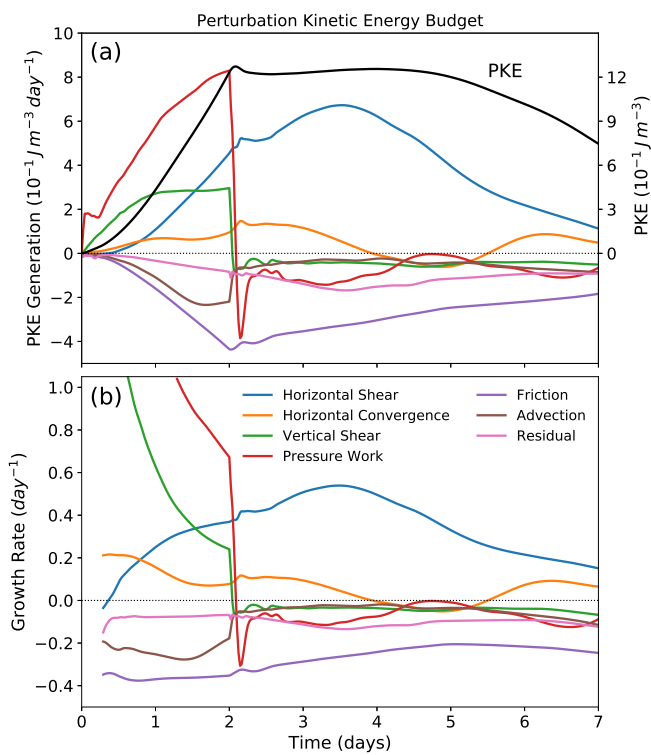

Figure 17. Terms in K_e budget (Eq. 14) for the simulation using the monsoon basic state. (a) total K_e production and (b) growth rates

Integrated Perturbation Kinetic Energy from 0 to 48 hrs (shading, Jm^{-3}) and $\vec{V}$ (vectors, 3.1 km)

(a) Horizontal Shear

(b) Horizontal Convergence

(c) Vertical Shear
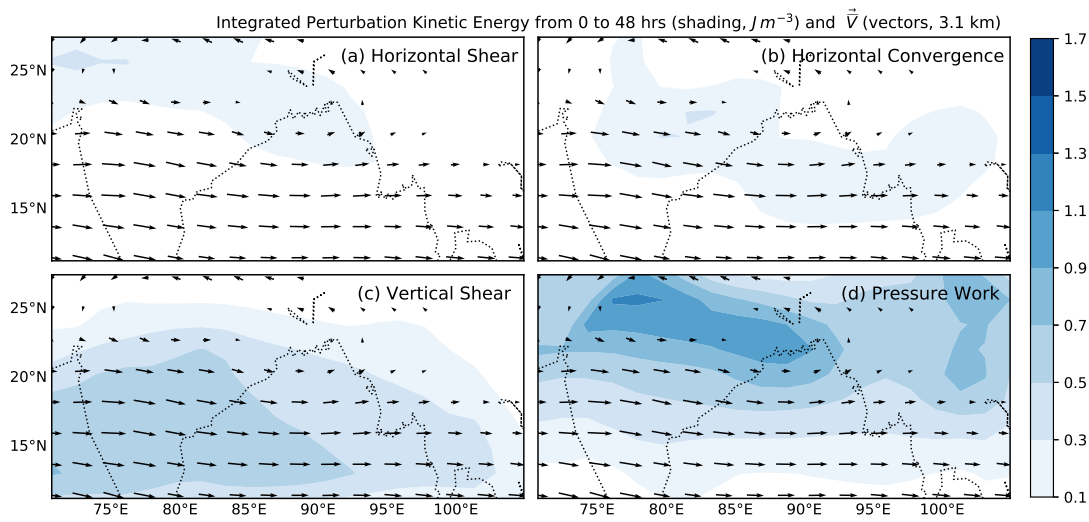
(d) Pressure Work

Figure 18. Total perturbation kinetic energy generated by select terms in Eq. 14 from 0 to 48 hours of each simulation. The numerical value for each of the 200 simulations is plotted at the center of the heating perturbation.
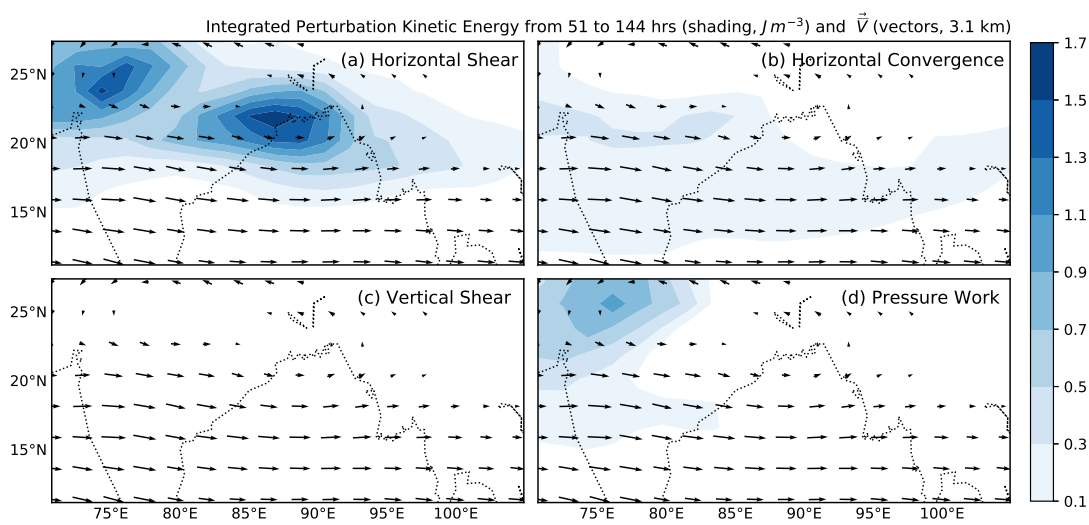

Integrated Perturbation Kinetic Energy from 51 to 144 hrs (shading, Jm^{-3}) and $\vec{V}$ (vectors, 3.1 km)

(a) Horizontal Shear

(b) Horizontal Convergence

(c) Vertical Shear

(d) Pressure Work

Figure 19. Same as in Fig. 18, but from 51 to 144 hours.